



Universiteit  
Leiden  
The Netherlands

## **Paving the path between low- and high-mass star formation : dynamics probed by Herschel far-infrared spectroscopy**

San Jose Garcia, I.

### **Citation**

San Jose Garcia, I. (2015, June 18). *Paving the path between low- and high-mass star formation : dynamics probed by Herschel far-infrared spectroscopy*. PhD Thesis. Retrieved from <https://hdl.handle.net/1887/33224>

Version: Not Applicable (or Unknown)

License: [Licence agreement concerning inclusion of doctoral thesis in the Institutional Repository of the University of Leiden](#)

Downloaded from: <https://hdl.handle.net/1887/33224>

**Note:** To cite this publication please use the final published version (if applicable).

Cover Page



Universiteit Leiden



The handle <http://hdl.handle.net/1887/33224> holds various files of this Leiden University dissertation

**Author:** San José García, Irene

**Title:** Paving the path between low- and high-mass star formation : dynamics probed by *Herschel* far-infrared spectroscopy

**Issue Date:** 2015-06-18

# 4

*Linking low- to high-mass YSOs with  
Herschel-HIFI observations of water*

*I. San José-García, J. C. Mottram, E. F. van Dishoeck, et al.  
submitted*

## Abstract

Water effectively probes the dynamics in young stellar objects (YSOs), especially shocks in molecular outflows. It is therefore a key molecule to explore whether the physical properties of low-mass protostars can be extrapolated to massive YSOs, an important step in understanding the fundamental mechanisms regulating star formation.

As part of the WISH key programme, we investigate excited water line properties as a function of source luminosity, in particular the dynamics and the excitation conditions of shocks along the outflow cavity wall. Velocity-resolved *Herschel*-HIFI spectra of the H<sub>2</sub>O 2<sub>02</sub>-1<sub>11</sub> (988 GHz), 2<sub>11</sub>-2<sub>02</sub> (752 GHz) and 3<sub>12</sub>-3<sub>03</sub> (1097 GHz) lines are analysed, together with <sup>12</sup>CO  $J = 10-9$  and 16-15, for 52 YSOs with bolometric luminosities ranging from  $< 1$  to  $> 10^5 L_{\odot}$ .

The H<sub>2</sub>O and <sup>12</sup>CO line profiles are decomposed into multiple Gaussian components which are related to the different physical structures of the protostellar system. The non-LTE radiative transfer code RADEX is used to constrain the excitation conditions of the shocks along the outflow cavity. The profiles of the three excited water lines are similar, indicating that they are probing the same gas. Two main emission components are seen in all YSOs: a broad component associated with non-dissociative shocks in the outflow cavity wall (“cavity shocks”) and a narrow component associated with the quiescent envelope material. More than 60% of the total integrated intensity in the excited water lines comes from the broad cavity shock component, while the remaining emission comes mostly from the envelope for low-mass Class I, intermediate- and high-mass objects and dissociative “spot shocks” for low-mass Class 0 protostars. The widths of the water lines are surprisingly similar from low- to high-mass YSOs, whereas <sup>12</sup>CO  $J = 10-9$  line widths increase slightly with  $L_{\text{bol}}$ . The excitation analysis of the cavity shock component shows stronger 752 GHz emission for high-mass YSOs, likely due to pumping by an infrared radiation field. Finally, a strong correlation with slope unity is measured between the logarithms of the total H<sub>2</sub>O line luminosity,  $L_{\text{H}_2\text{O}}$ , and  $L_{\text{bol}}$ , which can be extrapolated to extragalactic sources.

The water emission probed by spectrally unresolved data is largely due to shocks. Broad water and high- $J$  CO lines originate in shocks in the outflow cavity walls for both low- and high-mass YSOs, whereas lower- $J$  CO transitions mostly trace entrained outflow gas. The higher UV field and turbulent motions in high-mass YSOs compared to their low-mass counterparts may explain the slightly different kinematical properties of <sup>12</sup>CO  $J = 10-9$  and H<sub>2</sub>O lines from low- to high-mass.

## 4.1. Introduction

The physical and chemical conditions present in low- and high-mass star forming regions differ significantly. Massive star forming regions are found to have higher UV radiation fields and levels of turbulence than their low-mass counterparts (see Stauber et al. 2007; Herpin et al. 2012). The temperatures, feedback mechanisms, magnetic fields, accretion rates and outflow forces are different between low- and high-mass young stellar objects (for more details see Bontemps et al. 1996; Behrend & Maeder 2001b; Beuther et al. 2002, 2007; Palla & Stahler 1993b; Cesaroni 2005; Zinnecker & Yorke 2007).

However, many studies have shown that high-mass YSOs behave in certain aspects as scaled-up versions of their low-mass counterparts (van der Tak et al. 1999, 2000; Shepherd 2003; Johnston et al. 2012; San Jose-Garcıa et al. 2013; Karska et al. 2014a, San Jose-Garcıa et al. subm.). In addition, the lifetime of the embedded phase of high-mass YSOs (0.07-0.4 Myrs, Mottram et al. 2011) is comparable to that of low-mass YSOs (0.15 Myr for Class 0, 0.5 Myr for Class 0+I, Dunham et al. 2014), even if massive objects evolve more in this period. The line luminosity of molecules like CO, HCO<sup>+</sup> and OH scales with bolometric luminosity and envelope mass as well as the degree of turbulence in the warmer inner regions of protostellar envelopes (San Jose-Garcıa et al. 2013; van der Tak et al. 2013; Wampfler et al. 2013; Benz et al. subm.). Moreover, the kinematics of outflows and envelopes seem to be linked independently of the mass of the forming star (San Jose-Garcıa et al. 2013). Therefore, a further characterisation of the physical conditions and dynamics of these components will help to identify the differences and similarities between low- and high-mass YSOs and better understand the fundamental processes in the formation of stars.

Water is unquestionably a key molecule to study the energetics and dynamical properties of protostellar environments (van Dishoeck et al. 2011). In particular, the analysis of the velocity resolved water data provided by the Heterodyne Instrument for the Far-Infrared (HIFI; de Graauw et al. 2010) on board of *Herschel* Space Observatory (Pilbratt et al. 2010) allows us to characterise the emission from molecular outflows, which play a crucial role in the formation of young stars and in the feedback on their surroundings (Kristensen et al. 2012; van der Tak et al. 2013; Mottram et al. 2014). Given the fact that the bulk of the water data on extragalactic sources out to the largest redshifts and the data provided by the other *Herschel* instruments (the Photodetector Array Camera and Spectrometer, PACS, Poglitsch et al. 2010; and the the Spectral and Photometric Imaging Receiver, SPIRE, Griffin et al. 2010) on galactic sources are spectrally unresolved, it is important to quantify the different components that make up the observed lines.

Outflows effectively remove angular momentum, necessary for the formation of a disk and mass accretion onto the forming star (see review by Lada & Kylafis 1999). The power agent of these structures (either jets or winds from the star/disk system) triggers not only the formation of the outflows, but also extreme and complex physical and chemical processes across the protostellar environment. In particular, different types of shocks take place in the outflow cavity wall, at the interface between the cavity and the envelope. Non-dissociative outflow-cavity shocks are localised along the outflow cavity wall (Visser et al. 2012; Kristensen et al. 2012; Mottram et al. 2014). On the other hand, dissociative shocks take place either along the jet, revealed through perturbations known as extremely high velocity components (EHV) (Bachiller et al. 1990; Tafalla et al. 2010), or at the base of the outflow cavity wall where the jet or wind impacts directly (Kristensen et al. 2012, 2013; Mottram et al. 2014). These shocks are also called spot shocks. Therefore, shocks and turbulent motions injected into the cavity wall propagating within this physical structure are products linked to the activity of the molecular outflow (Arce et al. 2007). The dynamical nature of these two phenomena (turbulence and shocks) is different and also differ from that characterising the entraining gas in classical outflows. To comprehensibly interpret the molecular emission of H<sub>2</sub>O and <sup>12</sup>CO within the outflow-cavity system it is important to investigate whether the dynamical properties of low-mass objects can be extrapolated to more massive YSOs.

This was one of the goals of the “Water In Star forming regions with *Herschel*” key programme (WISH; van Dishoeck et al. 2011), which observed several water lines as well as high-*J* CO and isotopologue transitions for a large sample of YSOs covering early evolutionary stages over a wide

range of luminosities. An extensive study has been performed on all HIFI water observations for low-mass protostars (Mottram et al. 2014) and for low-lying water transitions within the high-mass sub-sample (van der Tak et al. 2013). The line profiles of the water transitions were analysed and decomposed into multiple velocity components, which are associated to different physical structures of the protostellar system. These studies investigated trends with luminosity, mass and evolution and explored the dynamical and excitation conditions probed by these lines. In addition, observations with PACS reveal that  $^{12}\text{CO } J>20$  transitions originate mostly in shocks for both low- and high-mass YSOs (Herczeg et al. 2012; Manoj et al. 2013; Green et al. 2013; Karska et al. 2013, 2014a,b). The excitation of warm CO is also similar across the luminosity range but rotational temperatures in high-mass objects are higher than in their low-mass counterparts in the case of  $\text{H}_2\text{O}$ , due to their higher densities (Karska et al. 2014a).

In order to link these two studies, this paper focuses on the analysis of the excited water lines across the entire WISH sample of YSOs. The ground-state water transitions of high-mass sources show absorption features from foreground clouds which complicates the extraction of velocity information from these lines (van der Tak et al. 2013), a reason why these lines are not considered in this study. Results from the line profile, line luminosity and excitation condition analysis are connected from low- to high-mass YSOs and interpreted together with those obtained from high- $J$   $^{12}\text{CO}$  observations ( $J \geq 10$ ). In addition, the obtained results may help to interpret and understand those of extragalactic sources. The aim is to better constrain the dynamical properties of molecular outflows across a large range of luminosities and complement the study presented in San José-García et al. (2013) based on the analysis of high- $J$  CO and isotopologue transitions for the same sample of YSOs.

We start by introducing the selected sample, the studied  $\text{H}_2\text{O}$  and  $^{12}\text{CO}$  observations and the reduction and decomposition methods in Sect. 4.2. The results from the water line profile and line luminosity analysis are presented in Sect. 4.3 and compared to those obtained for CO. In this section, the excitation conditions are also derived from the line intensity ratios. The interpretation of these results are discussed in Sect. 4.4, and extrapolated to extragalactic sources. Finally, in Sect. 4.5 we summarise the main conclusions of this work.

## 4.2. Observations

### 4.2.1. Sample

The sample of 51 YSOs is drawn from the WISH survey and is composed of 26 low-mass, six intermediate-mass and 19 high-mass YSOs. In addition, the intermediate-mass object OMC-2 FIR 4 (Kama et al. 2013) taken from the “Chemical *HERschel* Surveys of Star forming regions” key programme (CHESS; Ceccarelli et al. 2010) is added to enlarge the number of sources of this sub-group. The intrinsic properties of each source such as coordinates, source velocity ( $v_{\text{LSR}}$ ), bolometric luminosity, distance ( $d$ ), and envelope mass ( $M_{\text{env}}$ ) can be found in Mottram et al. (2014), Wampfler et al. (2013) and van der Tak et al. (2013) for the low-, intermediate- and high-mass YSOs respectively.

The sample covers a large interval of luminosity and each sub-group of YSOs contains a mix of different evolutionary stages: both low- and intermediate-mass objects range from Class 0 to Class I; and the high-mass YSOs from mid-IR-quiet/mid-IR-bright massive young stellar objects (MYSOs) to ultra-compact H II regions (UC H II). The focus of this paper is to analyse different physical properties across the luminosity range; trends within the low-mass sample are discussed in Mottram et al. (2014); the intermediate- and high-mass samples are too small to search for trends within their several evolutionary stages.

### 4.2.2. Water observations

The targeted para- $\text{H}_2\text{O } 2_{02-1_{11}}$  (988 GHz) and  $2_{11-2_{02}}$  (752 GHz) lines and the ortho- $\text{H}_2\text{O } 3_{12-3_{03}}$  (1097 GHz) line were observed with the HIFI instrument. The upper energy level ( $E_u$ ),

Table 4.1: Overview of the main properties of the observed water lines with HIFI.

Mol.	Trans.	$E_u/k_B$ (K)	Frequency (GHz)	Inst.-band	$\eta_{MB}^a$	$\theta^a$ (")	Spec. Resol. (km s <sup>-1</sup> )	Correction factor <sup>b</sup>
p-H <sub>2</sub> O	2 <sub>02</sub> -1 <sub>11</sub>	100.8	987.927	HIFI-4a	0.74	21.5	0.15	0.865
p-H <sub>2</sub> O	2 <sub>11</sub> -2 <sub>02</sub>	136.9	752.033	HIFI-2b	0.75	28.2	0.20	0.853
o-H <sub>2</sub> O	3 <sub>12</sub> -3 <sub>03</sub>	249.4	1097.365	HIFI-4b	0.74	19.3	0.14	0.865

**Notes.** <sup>(a)</sup> Parameters calculated using equations 1 and 3 of Roelfsema et al. (2012), respectively. <sup>(b)</sup> Beam efficiency correction factors of each excited water lines according to the updated values of  $\eta_{MB}$  for the different HIFI-bands.

frequency, HIFI-band, beam efficiency ( $\eta_{MB}$ ), beam size ( $\theta$ ) and spectral resolution of each water transition are given in Table 4.1. The beam efficiencies of the different HIFI-bands have been recently updated<sup>1</sup> and in general the values decrease by 15–20% for the band considered here. The presented observations have not been corrected with the new  $\eta_{MB}$  parameters because the analysis in this paper was completed before the new numbers were available and for consistency with our previous CO study. For completeness, the new beam correction factor of each HIFI-band are listed in Table 4.1.

The H<sub>2</sub>O 2<sub>02</sub>-1<sub>11</sub> line was observed for the entire WISH sample; the 2<sub>11</sub>-2<sub>02</sub> line for 24 out of the 26 studied low-mass protostars and for all intermediate- and high-mass YSOs; and the 3<sub>12</sub>-3<sub>03</sub> transition was observed for only 10 low-mass protostars, two out of six intermediate-mass sources and all high-mass YSOs. These water lines are detected for all observed intermediate- and high-mass YSOs and for 75% of the low-mass protostars (see Mottram et al. 2014).

The data were observed simultaneously by the Wide Band Spectrometer (WBS) and the High Resolution Spectrometer (HRS), in both vertical (V) and horizontal (H) polarisation (more details in Roelfsema et al. 2012). We present the WBS data because the baseline subtraction for the HRS data becomes less reliable due to the width of the water lines, which is comparable to the bandwidth of the HRS setting. Single pointing observations were performed for all targets in dual-beam-switch (DBS) mode with a chop throw of 3'. Contamination from emission by the off-position has only been identified in the H<sub>2</sub>O 2<sub>02</sub>-1<sub>11</sub> spectrum of the low-mass protostar BHR71 (further information in Mottram et al. 2014). The allocated observation numbers for each source and line, designated with the initial obsIDs, are indicated in Table A.2 of Mottram et al. (2014) for the low-mass protostars, and in Table 4.6 of this manuscript for the intermediate- and high-mass YSOs.

### 4.2.3. Additional <sup>12</sup>CO observations

Complementing the water observations, <sup>12</sup>CO  $J = 10-9$  and  $16-15$  spectra are included in this study to extend the comparison to other components of the protostellar system traced by this molecule and set a reference for abundance studies. The  $J = 10-9$  transition was observed as part of the WISH key programme for the entire low- and intermediate-mass sample and for the high-mass object W3-IRS5 (see San José-García et al. 2013). The  $J = 10-9$  spectrum was obtained for AFGL 2591 from the work of Kaźmierczak-Barthel et al. (2014). For the other high-mass sources, <sup>12</sup>CO  $J = 3-2$  spectra are used as a proxy (San José-García et al. 2013).

<sup>12</sup>CO  $J = 16-15$  observations of 13 low-mass Class 0 protostars were observed within the *Herschel* programme OT2\_ikrist01\_2 (Kristensen et al. in prep.). Finally, this transition was obtained for three high-mass YSOs: W3-IRS5 (OT2\_swampfle\_2 *Herschel* programme; Wampfler et. al 2014), and for AFGL 2591 (Kaźmierczak-Barthel et al. 2014) and NGC6334-I (Zernickel et al. 2012) as part of the CHESS key programme (Ceccarelli et al. 2010).

<sup>1</sup>Further information regarding the updated beam efficiencies values is presented in the technical note “Measured beam efficiencies on Mars (revision v1.1, 1 October 2014)” of the HIFI wiki page:

<http://herchel.esac.esa.int/twiki/bin/view/Public/HifiCalibrationWeb?template=viewprint>

#### 4.2.4. Reduction of the H<sub>2</sub>O data

The calibration process of the water observations was performed in the *Herschel* Interactive Processing Environment (HIPE<sup>2</sup>; Ott 2010) using version 8.2 or higher. The intensity was first converted to the antenna temperature  $T_A^*$  scale and velocity calibrated with a  $v_{\text{LSR}}$  precision of a few  $\text{m s}^{-1}$ . Further reduction was performed with the GILDAS-CLASS<sup>3</sup> package. The spectra observed in the H and V polarisations were averaged together to improve the signal-to-noise ratio ( $S/N$ ) and the intensity scale converted to main-beam brightness temperature scale,  $T_{\text{MB}}$ , using the specific beam efficiencies for each band (Roelfsema et al. 2012). Finally, a constant or linear baseline was subtracted.

All data were then resampled to  $0.27 \text{ km s}^{-1}$  in order to compare the results among the water lines and to those from the high- $J$  CO lines (San José-García et al. 2013) in a systematic manner. The rms noise of the spectra at that resolution, the maximum peak brightness temperature,  $T_{\text{MB}}^{\text{peak}}$ , the integrated intensity,  $W = \int T_{\text{MB}} dv$ , and the full width at zero intensity,  $FWZI$ , are presented in Tables 4.7 to 4.9. The latter parameter was measured as in Mottram et al. (2014): first by resampling all spectra to  $3 \text{ km s}^{-1}$  to improve the  $S/N$ , then re-calculating the rms and finally considering the “zero intensity” where the intensity of the spectrum drops below  $1\sigma$  of that rms. The velocity range constrained by the  $FWZI$  is used to define the limits over which the integrated intensity of the line is calculated.

Since the spectra have not been corrected with the recently released beam efficiencies of the different HIFI-bands<sup>1</sup> (Sect. 4.2.2), the results presented in Tables 4.7 to 4.9, as well as those shown in Figs. 4.3 and 4.9, should be divided by the correction factor indicated in Table 4.1. The line profiles do not change if the new  $\eta_{\text{MB}}$  values are applied and the variation of the line ratios is of the order of 1%.

Finally, the C<sup>18</sup>O  $J = 10-9$  emission line is detected in the line wing of the H<sub>2</sub>O  $3_{12}-3_{03}$  spectrum for five low-mass protostars (NGC 1333 IRAS2A and IRAS4B, Ser SMM1, GSS30 and Elias 29) and four high-mass YSOs (G5.89-0.39, W3-IRS3, NGC6334-I and W51N-e1). Therefore, a Gaussian profile with the same  $FWHM$ , position and amplitude as those constrained in San José-García et al. (2013) was used to remove the contribution of C<sup>18</sup>O  $J = 10-9$  line from the reduced H<sub>2</sub>O  $3_{12}-3_{03}$  spectrum for each of these sources. The data of these specific YSOs are then analysed and plotted after subtracting the C<sup>18</sup>O line.

#### 4.2.5. Decomposition method

As shown by Kristensen et al. (2010, 2012), van der Tak et al. (2013) and Mottram et al. (2014), the water line profiles are complex and can be decomposed into multiple velocity components. The purpose of decomposing the line profile is to disentangle the different regions probed within the protostar, which are characterised by specific physical conditions and kinematics.

Generally, these velocity components can be well reproduced by Gaussian-like profiles; other types of profiles do not give improved fits (Mottram et al. 2014). Depending on the water transition and luminosity of the source, the number of components needed to fit the profile varies. For most of the low-mass protostars, the spectra can be decomposed into a maximum of four different Gaussian components, as shown in Kristensen et al. (2010, 2012, 2013) and Mottram et al. (2014). In order to determine the number of velocity components of the water lines for the intermediate- and high-mass YSOs, these spectra were initially fit with one Gaussian profile using theIDL function *mpfitfun*. Then, the residual from this fit was analysed and since it was larger than 3 sigma rms for all lines, an extra Gaussian component was added to the decomposition method to improve the fitting. The procedure is the same but now considering two independent Gaussian profiles. A self-absorption feature at the source velocity was detected in the H<sub>2</sub>O  $2_{02}-1_{11}$  line for 9 out of 19 high-mass objects, so for those objects an extra Gaussian component in absorption was added in the decomposition

<sup>2</sup>HIPE is a joint development by the Herschel Science Ground Segment Consortium, consisting of ESA, the NASA Herschel Science Centre, and the HIFI, PACS and SPIRE consortia.

<sup>3</sup><http://www.iram.fr/IRAMFR/GILDAS/>



method. In some high-mass sources this component is weaker or non-detected in the other studied transitions and it can be negligible (for an example, see the DR21(OH) observations). Therefore, the number of components is determined by the spectrum itself and its  $S/N$  and not by the assumed method.

As in Mottram et al. (2014), we force the  $FWHM$  and central position of each component to be the same for all transitions and they are constrained simultaneously by all spectra of a given source. The intensities of each Gaussian component are free parameters that can vary for each water line. The resulting fits were examined visually as a sanity check. The values of the  $FWHM$ ,  $T_{\text{peak}}$ ,  $\nu_{\text{peak}}$ , and integrated intensity of each Gaussian component are summarised in Appendix 4.A, Tables 4.10 to 4.12.

#### 4.2.6. Association with physical components

The multiple velocity components needed to reproduce the  $\text{H}_2\text{O}$  line profiles can be related to physical components in protostellar systems (Kristensen et al. 2011, 2012; van der Tak et al. 2013; Mottram et al. 2014).

Quiescent inner envelope gas produces a Gaussian profile in emission with the smallest  $FWHM$  centred at the source velocity (see Sect. 3.2.2 of Mottram et al. 2014). In previous studies these velocity components were called narrow components. The cold outer protostellar envelope can cause a self-absorption, which is more common in ground-state  $\text{H}_2\text{O}$  lines and in objects with massive and cold envelopes (e.g. van der Tak et al. 2013, Mottram et al. 2013).

The chemical and physical conditions present in shocks increase the abundance of  $\text{H}_2\text{O}$  by sputtering from the grain mantles (Codella et al. 2010; Van Loo et al. 2013; Neufeld et al. 2014). The line profile resulting from shocked water emission depends on the nature and kinematical properties of the shocks generating it, which translate into velocity components with different features (see Table 3 and Sect. 3.2 of Mottram et al. 2014).

The emission from non-dissociative shocks in layers along the outflow cavity wall produces velocity components with the largest  $FWHM$  ( $>20 \text{ km s}^{-1}$ ) and are generally centred near the source velocity (Kristensen et al. 2010, 2013; van Kempen et al. 2010; Nisini et al. 2010; Suutarinen et al. 2014; Santangelo et al. 2014). However, these broad Gaussian-like profiles, named cavity shock components (Mottram et al. 2014) or simply broad components, should be differentiated from the broad velocity component identified in low- and mid- $J$  ( $J < 10$ ) CO spectra, even if shape and width are similar. The reason is that the water emission originates in shocks in the cavity while the CO emission comes from cooler material deeper in the wall and closer to the quiescent envelope (Raga et al. 1995; Yıldız et al. 2013).

In contrast, spot shocks occur in small localised regions and are associated to hotter and more energetic dissociative shocks (Mottram et al. 2014). This emission may originate in extremely-high velocity (EHV) gas along the jets (Bachiller et al. 1990; Tafalla et al. 2010; Kristensen et al. 2011) or at the base of the outflow cavity (previously referred to as either the medium or the offset component; Kristensen et al. 2013). These Gaussian profiles show smaller  $FWHMs$  than those measured for the cavity shock component and are in general more offset from the source velocity. A more detailed characterisation and discussion can be found in Mottram et al. (2014), van der Tak et al. (2013) and Kristensen et al. in prep.

The contribution of the cavity shock and envelope components with respect to the total integrated intensity of the water lines for the intermediate- and high-mass YSOs are presented in Table 4.2 together with the values for the low-mass Class 0 and Class I protostars calculated by Mottram et al. (2014). Table 4 of that manuscript shows the results for different water lines as well as the fraction corresponding to the spot shock component.

In the following, the different velocity components of the  $\text{H}_2\text{O}$  and CO lines are distinguished based on the probable physical origin of the emission and the width of the profile.

Table 4.2: Average fraction of the integrated intensity that the envelope and cavity shock components contribute to the total integrated intensity of the H<sub>2</sub>O 2<sub>02</sub>-1<sub>11</sub> (988 GHz), 2<sub>11</sub>-2<sub>02</sub> (752 GHz) and 3<sub>12</sub>-3<sub>03</sub> (1097 GHz) lines.

	H <sub>2</sub> O 2 <sub>02</sub> -1 <sub>11</sub>		H <sub>2</sub> O 2 <sub>11</sub> -2 <sub>02</sub>		H <sub>2</sub> O 3 <sub>12</sub> -3 <sub>03</sub>	
	$W_{\text{envelope}}/W_{\text{tot}}^a$	$W_{\text{cavity shock}}/W_{\text{tot}}$	$W_{\text{envelope}}/W_{\text{tot}}^a$	$W_{\text{cavity shock}}/W_{\text{tot}}$	$W_{\text{envelope}}/W_{\text{tot}}^a$	$W_{\text{cavity shock}}/W_{\text{tot}}$
LM0	0.0 ± 0.1	0.7 ± 0.1	0.0 ± 0.1	0.7 ± 0.1	0.0 ± 0.1	0.8 ± 0.1
LMI	0.2 ± 0.1	0.8 ± 0.1	0.3 ± 0.2	0.7 ± 0.2	0.0 ± 0.1	1.0 ± 0.1
IM	0.3 ± 0.1	0.6 ± 0.2	0.4 ± 0.2	0.6 ± 0.2	0.3 ± 0.1	0.6 ± 0.1
HM	0.4 ± 0.2	0.6 ± 0.2	0.4 ± 0.2	0.6 ± 0.2	0.4 ± 0.1	0.6 ± 0.1

**Notes.** LM0: low-mass Class 0 protostars; LMI: low-mass Class I sources; IM: intermediate-mass YSOs; HM: high-mass objects.

<sup>(a)</sup> As in Mottram et al. (2014), the envelope fraction,  $W_{\text{envelope}}$ , is calculated subtracting the cavity and spot shock contribution from the total integrated intensity,  $W_{\text{tot}}$ , for each water line, i.e.  $W_{\text{envelope}} = W_{\text{tot}} - W_{\text{cavity shock}} - W_{\text{spot shock}}$ .

## 4.3. Results

The basic properties of the spectra and their decomposition are introduced in Sect. 4.3.1. In Sect. 4.3.2 the results of the line profile decomposition are compared to those obtained for the high- $J$  CO observations described in San José-García et al. (2013). The water line luminosity properties are also compared to those of CO in Sect. 4.3.3. In Sect. 4.3.4 integrated intensity ratios calculated for different pairs of water transitions are presented and these line ratios are further studied as across the line profiles in Sect. 4.3.5. Finally, the excitation conditions of the water lines are analysed with the non-LTE radiative transfer code RADEX in Sect. 4.3.6.

### 4.3.1. Water line profile characterisation

The observed H<sub>2</sub>O 2<sub>02</sub>-1<sub>11</sub>, 2<sub>11</sub>-2<sub>02</sub>, and 3<sub>12</sub>-3<sub>03</sub> spectra for the intermediate- and high-mass YSOs are presented in Appendix 4.A, Figs. 4.11, 4.12 and 4.13, respectively. The Gaussian profile fitting the broad (cavity shock) component of each water transition and source is indicated with a pink line. The spectra of the low-mass protostars are shown in Appendix A of Mottram et al. (2014).

In order to easily compare all the data, normalised averaged spectra of the H<sub>2</sub>O 2<sub>02</sub>-1<sub>11</sub>, 2<sub>11</sub>-2<sub>02</sub> and 3<sub>12</sub>-3<sub>03</sub> transitions are computed for the low-mass Class 0 and Class I protostars, the intermediate-mass sources and high-mass YSOs, as shown in the three first panels of Fig. 4.1. These spectra are calculated for each transition by normalising each spectrum to its peak intensity and averaging it together with the observations of the corresponding sub-group of objects. The normalised averaged spectra obtained for the three H<sub>2</sub>O transitions are similar for each sub-type of YSOs. Only the H<sub>2</sub>O 2<sub>02</sub>-1<sub>11</sub> high-mass averaged spectrum shows a slightly different profile with respect to the other two water lines due to the presence of a self-absorption feature in some sources. Without considering the Class I protostars, the averaged spectrum for a given transition seems to be broader for the low-mass objects, but at the base of the spectra the widths are similar, independent of the luminosity.

In the right-hand panel of Fig. 4.1 the three H<sub>2</sub>O transitions (2<sub>02</sub>-1<sub>11</sub> in orange, 2<sub>11</sub>-2<sub>02</sub> in blue and 3<sub>12</sub>-3<sub>03</sub> in red) are over-plotted for four different sources: a low-mass Class 0 (NGC1333 IRAS 4B), a low-mass Class I (GSS 30 IRS), an intermediate-mass objects (NGC2071) and a high-mass YSO (W33A). For each source, the shapes of the three water line profiles are similar but scaled-up in intensity, a result that is confirmed from the visual inspection of the water line profiles of all YSOs. In particular, the line wings are very similar. This indicates that the three water transitions are probing the same dynamical properties in each source.

Moving to the outcomes from the line decomposition explained in Sect. 4.2.5, the analysis suggests that the quiescent envelope and cavity shock components are the only two physical components consistently present in the H<sub>2</sub>O 2<sub>02</sub>-1<sub>11</sub>, 2<sub>11</sub>-2<sub>02</sub> and 3<sub>12</sub>-3<sub>03</sub> spectra of all low-, intermediate-

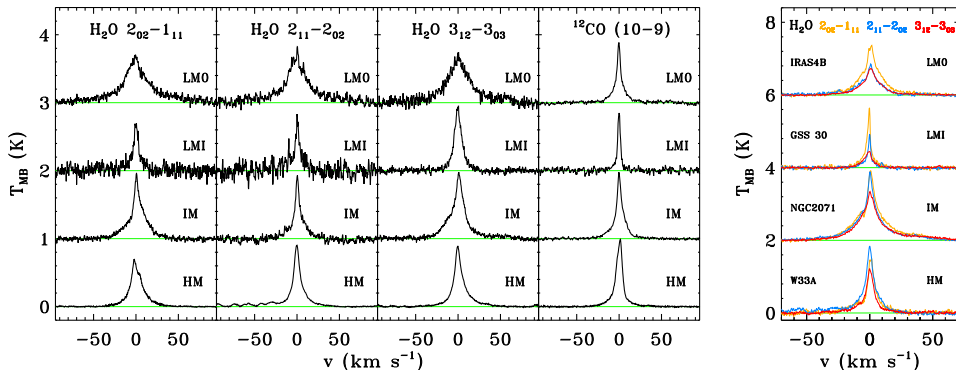


Figure 4.1: *Left* figure: Averaged and normalised spectrum calculated for the low-mass Class 0 (LM0) protostars, the low-mass Class I (LMI), intermediate-mass YSOs (IM) and high-mass objects (HM) for the  $\text{H}_2\text{O } 2_{02}-1_{11}$  988 GHz (*left* panel),  $2_{11}-2_{02}$  752 GHz (*middle-left* panel),  $3_{12}-3_{03}$  1097 GHz (*middle-right* panel) transitions and the  $^{12}\text{CO } J = 10-9$  (*right* panel) spectra (see San José-García et al. 2013). The low intensity features on the blue wing of the  $\text{H}_2\text{O } 2_{11}-2_{02}$  high-mass profile are due to methanol emission. *Right* figure:  $\text{H}_2\text{O } 2_{02}-1_{11}$ ,  $2_{11}-2_{02}$  and  $3_{12}-3_{03}$  spectra plotted in orange, blue and red respectively for NGC 1333 IRAS4B (LM0), GSS 30 (LMI), NGC2071 (IM) and W33A (HM). All spectra have been shifted to zero velocity and the horizontal light green lines in both figures represent the baseline level.

and high-mass YSOs. The spot shock components are not detected for the excited water lines presented here towards high-mass YSOs and six out of seven intermediate-mass objects, though they have been seen in absorption against the outflow in some ground-state  $\text{H}_2\text{O}$  lines for some high-mass sources (for more information see van der Tak et al. 2013).

As shown in Table 4.2, for a given sub-sample of YSOs the averaged contribution of the cavity shock component with respect to the total integrated intensity of the line is the same for the three water transitions. This fraction seems to decrease from low- to high-mass, but no statistically significant trend with  $L_{\text{bol}}$  can be claimed because the specific contribution of the cavity shock emission varies from source to source. The remaining emission comes from the envelope in the case of the low-mass Class I, intermediate- and high-mass YSOs and from spot shock components for low-mass Class 0 protostars (Mottram et al. 2014). This picture is consistent with the average spectra presented in Fig. 4.1, where the envelope component of the water lines is more prominent for the high-mass sources than for their low-mass Class 0 counterparts.

Independently of these numbers, in this paper we focus on characterising the physical conditions causing the line-wing emission in the water line profiles, i. e., the broader velocity component associated to the shock emission along the outflow cavity.

### 4.3.2. Comparison of the $\text{H}_2\text{O}$ and $^{12}\text{CO}$ line profiles

The fourth panel in Fig. 4.1 includes the normalised averaged  $^{12}\text{CO } J = 10-9$  spectrum of each sub-sample of YSOs. These averaged profiles are clearly narrower than those of water, especially for the low-mass Class 0 protostars, and the width of the spectra seems to increase from low- to high-mass. Therefore, just from a basic visual inspection of the water and the high- $J$  CO normalised averaged spectra we can point to differences in the shape of the line profiles of these two molecules and a different trend in the width from low- to high-mass.

To consistently compare the dynamical conditions of the entrained outflowing material traced by CO and the shocked gas along the outflow cavity, the line-wing emission of these two species is analysed using two parameters: the  $FWHM$  and the  $FWZI$  (see Sections 4.2.4 and 4.2.5). Both variables are used because  $FWHM$  characterises the average extent of emission from the source velocity while  $FWZI$  characterises the fastest material. For simplification, the  $FWHM$  of the

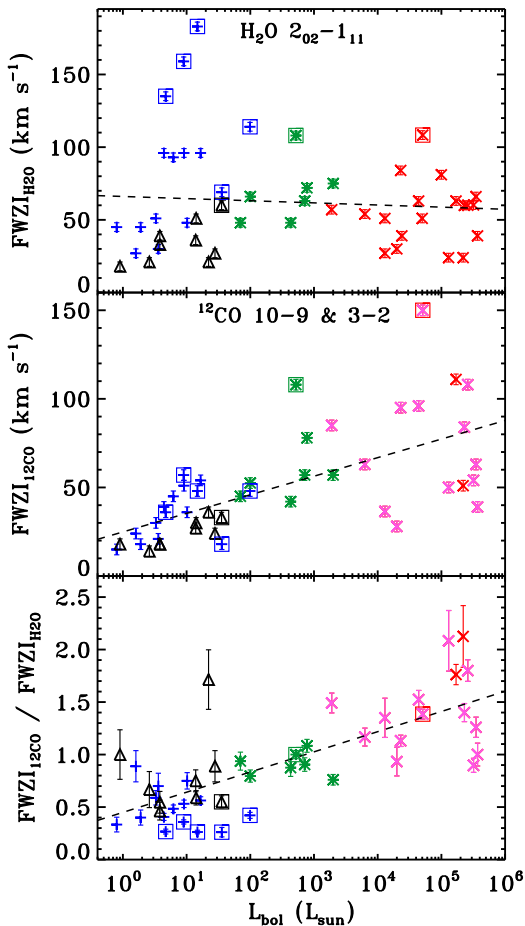


Figure 4.2: (*Top*)  $FWZI$  of the  $\text{H}_2\text{O } 2_{02}-1_{11}$  (988 GHz) emission line versus the bolometric luminosity. (*Middle*) Same as *top* panel but for the  $^{12}\text{CO } J = 10-9$  and  $J = 3-2$  observations. (*Bottom*) Ratio of the  $^{12}\text{CO}$  and  $\text{H}_2\text{O } 2_{02}-1_{11}$   $FWZI$  values as a function of  $L_{\text{bol}}$ . The blue plus symbols correspond to the low-mass Class 0 protostars, the black triangles the low-mass Class I, the green asterisks the intermediate-mass objects, the pink crosses the high-mass YSOs for which the  $^{12}\text{CO } J = 3-2$  spectra are used, and the red cross symbols the high-mass object for which  $^{12}\text{CO } J = 10-9$  data are available (see San José-García et al. 2013). The low- and intermediate-mass sources with detected EHV components are surrounded by a box, as well as the high-mass YSO with triangular water line profiles.

Gaussian profile reproducing the cavity shock component is differentiated from the other velocity components by using the sub-script  $b$  to indicate that this is the broader velocity component obtained from the line decomposition.

The top panel of Fig. 4.2 shows the  $FWZI$  for the  $\text{H}_2\text{O } 2_{02}-1_{11}$  transition as a function of bolometric luminosity (in Fig. 4.15 the  $FWZI$  of the other water lines are also plotted versus  $L_{\text{bol}}$  and envelope mass). Similarly, the constrained  $FWHM_b$  from the cavity shock component (same for all three lines) versus  $L_{\text{bol}}$  and  $M_{\text{env}}$  are presented in Fig. 4.14. The  $FWZI$  values vary from 15 to 189  $\text{km s}^{-1}$ , while the  $FWHM_b$  range from 13 to 52  $\text{km s}^{-1}$ . Due to the large scatter and dispersion of the data points, no trend or correlation with luminosity can be claimed in either case. The smaller  $FWZI$  and  $FWHM_b$  values are those of the low-mass Class I protostars, consistently lying at the bottom of these figures. In addition, the low- and intermediate-mass YSOs which show EHV components are marked with squares in Fig. 4.2 to indicate that their  $FWZI$  was calculated including the spot shock emission and to investigate if there is any particular trend for these objects. The spectra of the marked high-mass object does not have EHV components but their line profiles are characterised with broad and triangular shapes. More information about these specific sources can be found in Appendix 4.B.

The  $FWZI$  and  $FWHM_b$  for the  $^{12}\text{CO}$  observations (middle panels of Figs. 4.2 and 4.14 respectively) are spread across a smaller velocity range than that for water. In addition, the  $FWZI$  shows less scatter than the  $FWHM_b$ . There is a statistically significant trend of larger  $FWZI$  for

Table 4.3: Averaged rms value in  $0.27 \text{ km s}^{-1}$  bin and mean (dash) values of the  $FWHM_b$  and  $FWZI$  for the three water lines and the  $^{12}\text{CO } J = 10-9$  spectra for each sub-type of YSO. The averaged  $FWHM_b$  and  $FWZI$  ratios calculated from the  $^{12}\text{CO}$  and  $\text{H}_2\text{O}$  observations are also indicated in the last two columns.

	H <sub>2</sub> O		2 <sub>02-111</sub>		2 <sub>11-202</sub>		3 <sub>12-303</sub>		<sup>12</sup> CO $J = 10-9$			<sup>12</sup> CO / H <sub>2</sub> O	
	$FWHM_b$ (km s <sup>-1</sup> )	$\sigma_{rms}$ (mK)	$FWZI$ (km s <sup>-1</sup> )	$\sigma_{rms}$ (mK)	$FWZI$ (km s <sup>-1</sup> )	$\sigma_{rms}$ (mK)	$FWZI$ (km s <sup>-1</sup> )	$FWHM_b$ (km s <sup>-1</sup> )	$\sigma_{rms}$ (mK)	$FWZI$ (km s <sup>-1</sup> )	$FWHM_b$	$FWZI$	
LM0	30 ± 12	23	86 ± 45	20	87 ± 47	17	86 ± 31	20 ± 9	112	36 ± 14	0.7 ± 0.3	0.5 ± 0.2	
LMI	18 ± 5	22	34 ± 13	17	33 ± 15	9	42 <sup>a</sup>	11 ± 1	115	24 ± 8	0.6 ± 0.1	0.8 ± 0.4	
IM	29 ± 5	24	69 ± 19	22	63 ± 30	19	79 <sup>a</sup>	20 ± 4	105	63 ± 21	0.7 ± 0.2	0.9 ± 0.1	
HM	27 ± 10	78	47 ± 10	68	70 ± 32	45	71 ± 35	22 <sup>a</sup>	180	81 ± 30 <sup>b</sup>	0.9 <sup>a</sup>	1.9 ± 0.2 <sup>b</sup>	

**Notes.** LM0: low-mass Class 0 protostars; LMI: low-mass Class I sources; IM: intermediate-mass YSOs; HM: high-mass objects.

See specification in the  $FWZI$  calculation for the low-mass objects in Mottram et al. 2014.

(<sup>a</sup>) No standard deviation is given because the number of observed or detected sources is less than four.

(<sup>b</sup>) For the high-mass YSOs, the  $^{12}\text{CO } J = 3-2$  spectra were included in the calculation of the mean value of the  $FWZI$  parameter.

more luminous sources ( $4.7\sigma^4$ ) with a Pearson correlation coefficient  $r = 0.72$ , which is also seen to a lesser extent for the  $FWHM_b$ .

Table 4.3 presents the mean  $FWHM_b$  and  $FWZI$  values for  $\text{H}_2\text{O}$  and  $^{12}\text{CO}$  and the averaged rms in a  $0.27 \text{ km s}^{-1}$  bin,  $\sigma_{rms}$ . In the case of the high-mass YSOs, the derived values are not affected by the higher  $\sigma_{rms}$  in those data (as left panels of Fig. 4.1 already show) since the actual signal to noise,  $S/N$ , on the water spectra themselves given by the peak intensity relative to the rms are higher (averaged  $S/N$  value of  $\sim 60$ ) than those of their low-mass counterparts (averaged  $S/N$  of  $\sim 20$ ).

Without considering the low-mass Class I protostars, which are more evolved and therefore have weaker, less powerful outflows (Mottram et al. 2014), the average  $FWHM_b$  and  $FWZI$  values derived for  $\text{H}_2\text{O}$  are similar from low- to high-mass (Table 4.3). A decrease of the mean  $FWZI$  values with increasing luminosity is only hinted for the  $\text{H}_2\text{O } 2_{02-111}$  transition. Combining the results from both  $FWHM_b$  and  $FWZI$  we conclude that the extent of the water line emission is similar for the entire sample. In contrast, and as suggested by the middle panel of Fig. 4.2, the averaged values of both  $FWZI$  and  $FWHM_b$  for the  $^{12}\text{CO}$  observations seem to increase with luminosity.

The dispersion observed for the  $FWZI$  and  $FWHM_b$  in both  $\text{H}_2\text{O}$  and  $\text{CO}$  could be related to the intrinsic properties of the source, such as its inclination, evolutionary stage, clustering, etc. In order to minimise possible effects caused by these inherent characteristics, the ratio of the  $FWZI$  derived for the  $^{12}\text{CO } J = 10-9$  and  $J = 3-2$  spectra and the  $FWZI$  of the water lines is plotted versus the bolometric luminosity in the bottom panel of Fig. 4.2. The same procedure is followed for  $FWHM_b$  of the  $^{12}\text{CO}$  and water spectra (see bottom panels of Fig. 4.14 in Appendix 4.C).

Independently of the use of  $FWZI$  or  $FWHM_b$ , a correlation between these ratios and  $L_{bol}$  is measured for each of the three water lines with statistical significance between  $3.3\sigma$  and  $5.0\sigma$  (Pearson correlation coefficients between 0.50 and 0.75). While  $^{12}\text{CO } J = 3-2$  and  $10-9$  may trace different layers in the outflow (Yildiz et al. 2013; Santangelo et al. 2013), the  $FWZI$ , i. e., the maximum offset velocity ( $v_{max}$ ), of the  $\text{CO}$  lines does not change with the  $J$  transition (Kristensen et al. in prep.). Therefore, the use of  $^{12}\text{CO } J = 3-2$  as a proxy for  $^{12}\text{CO } J = 10-9$  for the high-mass sources will not affect this trend.

The average ratios of  $FWZI$  and  $FWHM_b$  are also given in Table 4.3 and generally increase with increasing  $L_{bol}$ . The  $FWZI$  ratio indicates that the velocity of the material traced by the wings of  $^{12}\text{CO}$  is larger than that of water for the high-mass YSOs. The  $FWHM_b$  values are basically

<sup>4</sup>The significance of a correlation for a given number of data points and Pearson correlation coefficient is calculated as described in Marseille et al. (2010).

Table 4.4: *Top half*: Slope ( $m$ ), intercept ( $n$ ), and Pearson correlation coefficient ( $r$ ) of the power-law fit to the correlation between the logarithm of the H<sub>2</sub>O line luminosity and the logarithm of the bolometric luminosity ( $L_{\text{bol}}$ , left-columns) and the logarithm of the envelope mass ( $M_{\text{env}}$ , right-columns). *Bottom half*: Same as above, but for the correlation between the luminosity corresponding to the cavity shock component and  $L_{\text{bol}}$  or  $M_{\text{env}}$ .

Line (GHz)	$\log(L_{\text{H}_2\text{O}}) = n + m \cdot \log(L_{\text{bol}})$			$\log(L_{\text{H}_2\text{O}}) = n + m \cdot \log(M_{\text{env}})$		
	$m$	$n$	$r$	$m$	$n$	$r$
988	$0.85 \pm 0.05$	$-3.48 \pm 0.14$	0.94	$1.19 \pm 0.05$	$-2.91 \pm 0.10$	0.96
752	$0.94 \pm 0.05$	$-3.59 \pm 0.18$	0.94	$1.30 \pm 0.06$	$-2.91 \pm 0.12$	0.96
1097	$0.76 \pm 0.05$	$-3.23 \pm 0.18$	0.95	$1.11 \pm 0.08$	$-2.94 \pm 0.18$	0.93
	$\log(L_{\text{broad H}_2\text{O}}) = n + m \cdot \log(L_{\text{bol}})$			$\log(L_{\text{broad H}_2\text{O}}) = n + m \cdot \log(M_{\text{env}})$		
988	$0.79 \pm 0.04$	$-3.43 \pm 0.14$	0.94	$1.11 \pm 0.05$	$-2.90 \pm 0.10$	0.96
752	$0.83 \pm 0.05$	$-3.37 \pm 0.18$	0.94	$1.15 \pm 0.06$	$-2.80 \pm 0.13$	0.95
1097	$0.73 \pm 0.05$	$-3.34 \pm 0.19$	0.95	$1.08 \pm 0.08$	$-3.06 \pm 0.18$	0.93

the same for <sup>12</sup>CO and H<sub>2</sub>O, independently of whether these molecules are probing different regions and physical conditions within the outflow. However, this is not the case for the low-mass protostars, which show larger line-wings for the water observations than for the <sup>12</sup>CO observations, consistent with Kristensen et al. (2012). This trend is further analysed and interpreted in Sect. 4.4.1.

### 4.3.3. Line luminosity study

The integrated intensity of the water emission lines,  $W = \int T_{\text{MB}} dv$ , is calculated as described in Sect. 4.2.4 and presented, together with its uncertainty, in Tables 4.7 to 4.9. For those H<sub>2</sub>O 2<sub>02</sub>-1<sub>11</sub> spectra with an absorption at the source velocity, the integrated intensity was determined by masking the absorption feature and using the area traced by the two Gaussian emission profiles fitting the spectrum.

Since the studied sample of YSOs covers a wide range of luminosities and distances (from 0.13 to 7.9 kpc), the integrated intensity is converted to line luminosity,  $L_{\text{H}_2\text{O}}$ . This parameter takes into account the distance and can be compared to values obtained in extragalactic studies. These quantities have been calculated using Eq. (2) of Wu et al. (2005), assuming a Gaussian beam with size according to Table 4.1 and point source objects. The uncertainties in the line luminosity are calculated from the rms of the spectrum and assuming a distance uncertainty of  $\sim 20\%$ .

Figure 4.3 presents the logarithm of the line luminosity for each water transition,  $\log(L_{\text{H}_2\text{O}})$ , versus the logarithm of the bolometric luminosity,  $\log(L_{\text{bol}})$ . A strong correlation between the logarithm of these quantities is measured (solid black line) for each of the three lines. The Pearson correlation coefficient,  $r$ , is larger than 0.9 and the trends extend over more than six orders of magnitude in both axes. Similarly, a strong correlation is also measured between the logarithm of  $L_{\text{H}_2\text{O}}$  and the logarithm of the envelope mass,  $M_{\text{env}}$  (see Fig. 4.17 in Appendix 4.C). The parameters of the fit and correlation coefficient for all water lines and for both  $L_{\text{bol}}$  and  $M_{\text{env}}$  are presented in Table 4.4.

The slope of the correlations are close to one within the uncertainty. As there is no saturation of the line luminosity, the emission must be optically thin or at least effectively thin (i.e. optically thick but sub-thermally excited, see Linke et al. 1977). In either case, the intensity scales as the product of the beam-averaged column density and average volume density in the emitting gas. Assuming that the density in the regions probed by water in low- and high-mass protostars are similar, a correlation between  $\log(L_{\text{H}_2\text{O}})$  and  $\log(L_{\text{bol}})$  with slope close to unity suggests that the emitting region size increases with  $L_{\text{bol}}$  such that the filling factor of the beam is approximately the same for all sources. The 3<sub>12</sub>-3<sub>03</sub> transition shows the smallest number of detections for the low-mass protostars, which could explain the difference in the value of the slope with respect the

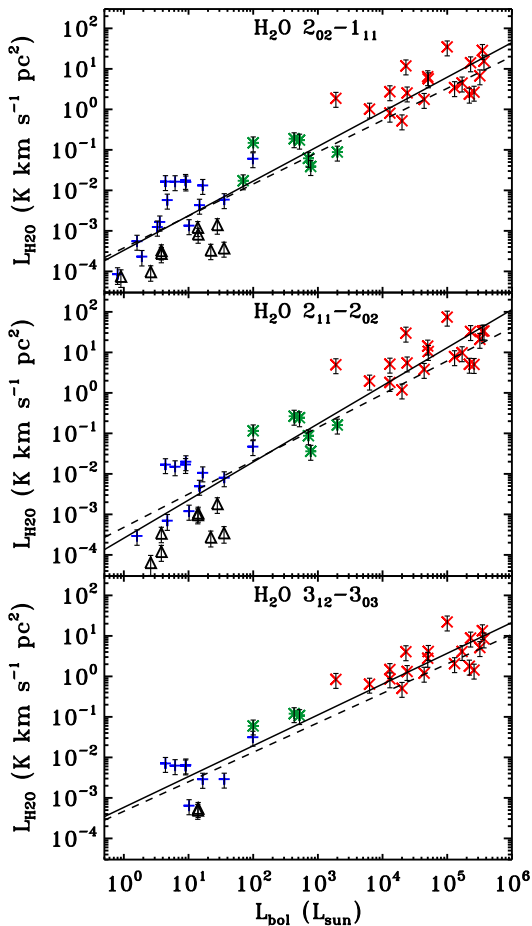


Figure 4.3: Line luminosity of the  $\text{H}_2\text{O } 2_{02}-1_{11}$  (988 GHz) line emission (*top*), the  $\text{H}_2\text{O } 2_{11}-2_{02}$  (752 GHz) data (*middle*), and  $\text{H}_2\text{O } 3_{12}-3_{03}$  (1097 GHz) spectra (*bottom*) versus the bolometric luminosity of the source. The blue pluses correspond to the low-mass Class 0 protostars, the black triangles the low-mass Class I, the green asterisks the intermediate-mass objects and the red cross symbols the high-mass YSOs. The solid line indicates the linear correlation of the logarithm of the total line luminosity,  $\log(L_{\text{H}_2\text{O}})$ , and  $\log(L_{\text{bol}})$ . The dashed line shows the log-log correlation of the luminosity measured for the broader Gaussian velocity component only (cavity shock emission;  $L_{\text{broad H}_2\text{O}}$ ) and  $\log(L_{\text{bol}})$ .

other two water lines. This linear correlation of  $\log(L_{\text{H}_2\text{O}})$  and  $\log(L_{\text{bol}})$  should not be extrapolated to the ground-based water transitions due to the presence of broad and deep absorption features which complicate the comparison of the water line luminosity, particularly in the case of massive YSOs (see van der Tak et al. 2013).

The same correlation between the  $^{12}\text{CO } 10-9$  line luminosity and  $L_{\text{bol}}$  was measured by San José-García et al. (2013, their Fig. 6). The calculated slope of the linear fit is the same within the uncertainty to those derived for the water lines (see Table 4 of San José-García et al. 2013, for comparison). As also noted by Mottram et al. (2014), the low-mass Class I sources have lower water line luminosities than the Class 0 sources, due to decreases in both  $FWHM$  and  $FWZI$  (see Table 2), as well as peak intensities, causing a clear separation between these two classes of low-mass protostars. However, in the case of CO, the separation between the low-mass Class 0 and Class I was small. Both  $^{12}\text{CO } J = 10-9$  and especially water are more sensitive to fast moving material in the outflows, which differentiate sources at different evolutionary stages, while the CO isotopologues are mostly probing the bulk of quiescent envelope material. This confirms the conclusions of Mottram et al. (2014) that the difference in water emission between Class 0 and Class I sources is related to the decreasing strength of the outflow and not to the removal of the envelope.

The integrated intensity emission coming from the cavity shocks, i. e., the area of the Gaussian profile fitting the line-wings, is also converted to line luminosity,  $L_{\text{broad H}_2\text{O}}$ . Figure 4.18 of Appendix 4.C shows the logarithm of this quantity as a function of  $\log(L_{\text{bol}})$ . As for the total line

luminosity, a strong correlation which extends across the entire luminosity range is measured but with slightly smaller values of the slope (averaged slope of  $0.78 \pm 0.04$ ). Figure 4.3 includes for each water transition the relation between the logarithm of  $L_{\text{broad H}_2\text{O}}$  and  $L_{\text{bol}}$  (dashed black line) for comparison with the total line luminosity,  $L_{\text{H}_2\text{O}}$ , (solid black line). The parameters from the log-log correlations of the broad component are also presented in Table 4.4. Consistent with the larger envelope contribution for high-mass sources (see Table 4.2) the differences between the fits for  $L_{\text{H}_2\text{O}}$  and  $L_{\text{broad H}_2\text{O}}$  are larger for all three lines for the high-mass sub-sample.

The fact that we found the same strong correlation between the parameters  $\log(L_{\text{bol}})$  and  $\log(L_{\text{H}_2\text{O}})$  or  $\log(L_{\text{broad H}_2\text{O}})$ , i.e., similar values for the slope close to unity, confirms that the total water line luminosity is dominated by the broad component (outflow cavity shocks).

#### 4.3.4. Integrated intensity ratios

The integrated intensity ratios of two different water transitions across the luminosity range can be used to analyse the excitation and physical conditions of protostellar systems. Mottram et al. (2014) show that there is little variation in line ratio between outflow-related components for the low-mass sample. They showed that the lines lie in the optically thick but effectively thin regime. This means that the water lines presented in that study are sub-thermally excited due to their high critical densities compared to the actual gas density of the emitting region. This condition lowers the chance of collisional de-excitation, so photons will scatter and eventually escape as if the lines were optically thin. We will extend this study to intermediate- and high-mass YSOs, first considering the total integrated intensity ratios and then focusing on just the cavity shock component.

The observations of the different water transitions have different beam sizes which must be corrected by the corresponding beam-size ratio,  $\theta_1/\theta_2$ . However, the correction depends on the size and shape of the emitting region within the protostellar system covered by each beam. If the emission comes from a point source, the correction factor is  $(\theta_1/\theta_2)^2$ ; if the emitting area is conical, meaning that it fills the beam in one axis and is point-like in the other, then the correction applied should be  $(\theta_1/\theta_2)$ ; and if the emitting region covers both axes the factor used is 1 (Tafalla et al. 2010). For the considered water lines, the maximum scaling correction would be 2.1, corresponding to a point-source scaling of the  $2_{11}\text{-}2_{02}$  (752 GHz) and  $3_{12}\text{-}3_{03}$  (1097 GHz) beams.

The emission from the excited water transitions for the low-mass protostars mostly comes from the outflow cavity, which extend beyond a single *Herschel* beam (see Nisini et al. 2010; Santangelo et al. 2012, 2014; Mottram et al. 2014). In this case, the emitting area could be taken as conical or even assumed to fill both beams. So, either the beam correction factor is  $(\theta_1/\theta_2)$  or 1 (or something in between for other, more complex geometries). For the intermediate- and high-mass YSOs it is more complicated to define the area covered by the beams as the larger distances mean that the outflows are often unresolved in the *Herschel* beam. For this reason, we consider the three scenarios introduced in the previous paragraph and the entire range of intensity ratios (applying the three possible beam correction factors) are evaluated together with the results obtained from their low-mass counterparts. The  $\theta_1/\theta_2$  value for each pair of water lines are indicated in Table 4.5.

The ratios of the total integrated intensity of  $\text{H}_2\text{O}$   $2_{11}\text{-}2_{02} / 2_{02}\text{-}1_{11}$ ;  $3_{12}\text{-}3_{03} / 2_{02}\text{-}1_{11}$ ; and  $3_{12}\text{-}3_{03} / 2_{11}\text{-}2_{02}$  are shown as a function of bolometric luminosity in the top-, middle- and bottom-left panels of Fig. 4.4, respectively. The value of these ratios without applying the beam corrections are indicated by filled dots. The dashed lighter line connected to each dot represents the value of the ratio after applying the larger beam size correction assumed for each sub-sample of objects:  $\theta_1/\theta_2$  linear correction for the low-mass protostars and  $(\theta_1/\theta_2)^2$  for the intermediate- and high-mass YSOs. Therefore, the lighter vertical lines illustrate the range of values that the integrated intensity ratio could take for each source depending on the shape of the emission region.

Figure 4.4 also shows the analytical ratios of the integrated intensity derived for two extreme scenarios: when both water lines are optically thin (purple dotted-dashed line) and when they are optically thick (orange dashed line). In both cases local thermodynamical equilibrium (LTE), an excitation temperature,  $T_{\text{exc}}$ , of 300 K and the same beam size for the compared transitions are assumed. The specific numbers corresponding to each regime for each pair of water lines are



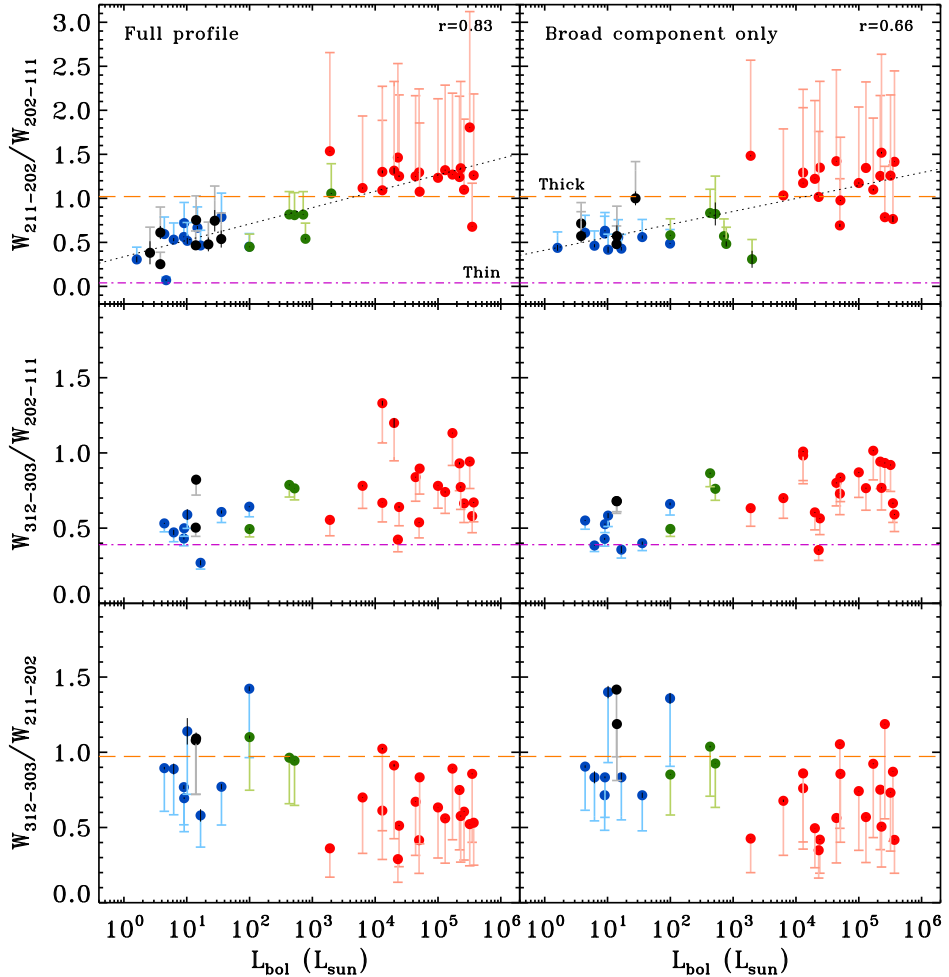


Figure 4.4: (*Top panels*) Ratio of the integrated intensities of the  $2_{11}-2_{02}$  (752 GHz) and  $2_{02}-1_{11}$  (988 GHz) water lines versus the bolometric luminosity of the source. (*Middle panels*) Ratio of the integrated intensities of the  $\text{H}_2\text{O}$   $3_{12}-3_{03}$  (1097 GHz) and  $2_{02}-1_{11}$  (988 GHz) spectra versus  $L_{\text{bol}}$ . (*Bottom panels*) Ratio of the integrated intensities of the  $3_{12}-3_{03}$  (1097 GHz) and  $2_{11}-2_{02}$  (752 GHz) water emission lines as a function of  $L_{\text{bol}}$ . The *left-column* presents the ratios calculated considering the entire line profile and the *right-column* shows the ratio of the integrated intensity calculated for the broad velocity component. The value of the ratios with and without correcting by the different beam size factors are indicated by dashed lighter lines and darker dot symbols respectively. Blue lines and symbols correspond to the low-mass Class 0 protostars, black to the low-mass Class I, green to intermediate-mass objects and red lines and symbols to high-mass YSOs. The purple dashed-dotted horizontal lines and the orange dashed horizontal lines indicate the optically thin and optically thick limits, respectively, calculated assuming LTE and an excitation temperature of 300 K. The linear correlation between the dot symbols (ratios not beam corrected) and the logarithm of the luminosity is shown by the dotted black lines in the *top panels*.

presented in Table 4.5. We take  $T_{\text{exc}} \approx 300$  K because this is the temperature found for the cavity shock component by (Mottram et al. 2014). Also, Karska et al. (2013, and references cited) observe with *Herschel* PACS a warm component for CO with an excitation temperature around 300 K and water is found to be spatially associated with this component in the outflow cavity (Santangelo et al. 2013). Note that for high densities, the excitation temperature approaches the kinetic temperature.

Table 4.5: Averaged values of H<sub>2</sub>O line intensity ratios for the shocked gas along the outflow cavity (broad component), beam size ratios of those transitions and the ratios of the optically thin and thick solutions at  $T_{\text{ex}}=300$  K.

Transitions	Observed ratio			$\theta_1/\theta_2$	Thin <sup>a</sup> (LTE)	Thick <sup>a</sup> (LTE)
	LM	IM	HM			
H <sub>2</sub> O 2 <sub>11</sub> -2 <sub>02</sub> /2 <sub>02</sub> -1 <sub>11</sub>	0.57 ± 0.14	0.60 ± 0.18	1.2 ± 0.2	1.31	0.04	1.02
H <sub>2</sub> O 3 <sub>12</sub> -3 <sub>03</sub> /2 <sub>02</sub> -1 <sub>11</sub>	0.52 ± 0.12	0.71 ± 0.16	0.8 ± 0.2	0.90	0.39	2.97
H <sub>2</sub> O 3 <sub>12</sub> -3 <sub>03</sub> /2 <sub>11</sub> -2 <sub>02</sub>	1.0 ± 0.3	0.94 ± 0.08	0.7 ± 0.2	0.68	3.16	0.97

**Notes.** LM: low-mass protostars; IM: intermediate-mass YSOs; HM: high-mass objects. The ratios are not corrected for different beam sizes.

<sup>(a)</sup> Line intensity ratio calculated for an excitation condition of 300 K and assuming LTE.

The ratio of the 2<sub>11</sub>-2<sub>02</sub> (752 GHz) and 2<sub>02</sub>-1<sub>11</sub> (988 GHz) transitions (top-left panel of Fig. 4.4) shows a significant increase with  $L_{\text{bol}}$ . The trend of the non-beam-corrected ratios (dots) is indicated by the dotted black line and confirmed by a Pearson correlation coefficient,  $r$ , equal to 0.83. This increase with luminosity is also seen when the maximum beam correction factor for each subgroup of YSOs (delineated by the dash) is applied ( $r = 0.85$ ). Therefore, the result is consistent across the luminosity range and regardless of emitting region shape. Furthermore, the intensity ratio of these H<sub>2</sub>O transitions is above 1 only for those sources with  $L_{\text{bol}} > 10^3 L_{\odot}$ .

The 3<sub>12</sub>-3<sub>03</sub> (1097 GHz) to 2<sub>02</sub>-1<sub>11</sub> (988 GHz) intensity ratio also seems to increase slightly with luminosity (middle-left panel Fig. 4.4). However, no trend can be claimed on a statistical basis because the significance of the Pearson correlation coefficient is less than  $2.5\sigma$  ( $r < 0.5$  and  $N = 32$ ). These ratios lie below 1 for all sources, independent of whether the beam correction factor has been applied (which is small for this combination of lines). The intensity ratio of the 3<sub>12</sub>-3<sub>03</sub> (1097 GHz) to 2<sub>11</sub>-2<sub>02</sub> (752 GHz) (bottom-left panel) is generally smaller than 1 for the three sub-sample of YSOs and it seems to decrease with  $L_{\text{bol}}$ . Once again, a trend cannot be claimed because the significance of this correlation is less than  $2.3\sigma$  ( $r < -0.5$  and  $N = 31$ ).

Comparison of the left and right panels of Fig. 4.4 show that similar results are obtained if the integrated intensity ratio corresponding to only the broad component is used for the same pair of water transitions as a function of  $L_{\text{bol}}$ . A trend with luminosity is also only observed for the 2<sub>11</sub>-2<sub>02</sub> / 2<sub>02</sub>-1<sub>11</sub> intensity ratio (with a smaller correlation coefficient  $r = 0.66$ ). The increase of the 2<sub>11</sub>-2<sub>02</sub> / 2<sub>02</sub>-1<sub>11</sub> ratio with  $L_{\text{bol}}$  suggests that the emission from the shocked gas along the outflow cavity becomes more excited, i.e., warmer and/or denser, for more massive objects. The 3<sub>12</sub>-3<sub>03</sub> / 2<sub>02</sub>-1<sub>11</sub> ratio seems to increase with  $L_{\text{bol}}$  while the 3<sub>12</sub>-3<sub>03</sub> / 2<sub>11</sub>-2<sub>02</sub> ratio decreases with luminosity, both of them tendencies not statistically significant.

The mean and standard deviation of the intensity ratios for the broad component are presented in Table 4.5, together with the beam size ratios and the estimated intensity ratios for the optically thin and thick solutions calculated assuming LTE and  $T_{\text{exc}} = 300$  K. These calculated values ratify the results and trends from low- to high-mass described in the previous paragraph.

We can rule out the optically thin LTE solution for all sources and lines, with the values for the 3<sub>12</sub>-3<sub>03</sub> / 2<sub>02</sub>-1<sub>11</sub> ratio excluding the optically thick LTE solution for both lines as well. In order to further constrain the excitation conditions, the non-LTE radiative transfer code `RADEX` will be used in Sect. 4.3.6.

### 4.3.5. Intensity ratios versus velocity for H<sub>2</sub>O and <sup>12</sup>CO

Here we investigate whether the excitation conditions change with velocity. Figure 4.5 shows the calculated line ratios of the H<sub>2</sub>O 2<sub>11</sub>-2<sub>02</sub> (752 GHz; top-panel) and 3<sub>12</sub>-3<sub>03</sub> (1097 GHz; bottom-panel) transitions over the 2<sub>02</sub>-1<sub>11</sub> (988 GHz) line as a function of velocity with respect to the source velocity. The grey shaded areas correspond to the averaged line ratio and standard deviation of the low-mass Class 0 protostars presented in Mottram et al. (2014). The green and red lines are

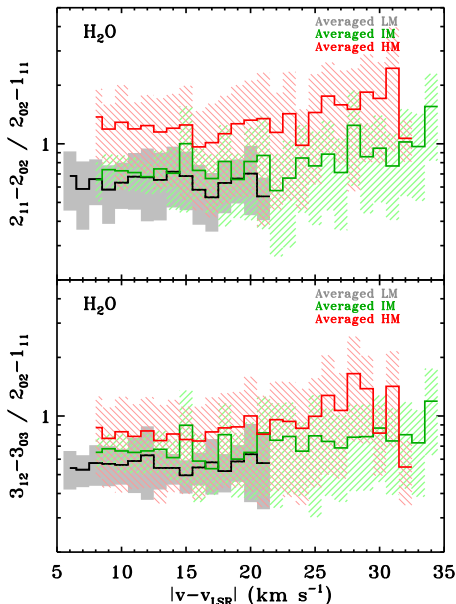


Figure 4.5: Averaged H<sub>2</sub>O  $2_{11-2_{02}} / 2_{02-1_{11}}$  ratio (*top* panel) and H<sub>2</sub>O  $3_{12-3_{03}}/2_{02-1_{11}}$  line intensity ratio (*bottom* panel) as a function of offset velocity for the low-mass protostars (LM; grey area from Mottram et al. 2014), intermediate-mass objects (IM; green line and asterisks), and the high-mass YSOs (HM; red line and crosses). The dashed green and red regions indicate the calculated standard deviation of the line ratio for each velocity channel.

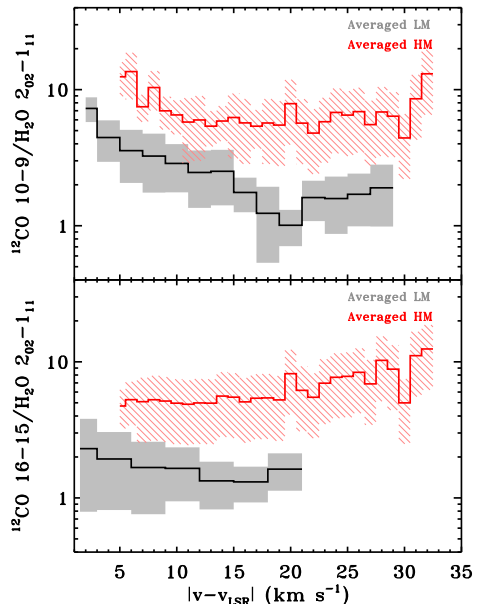


Figure 4.6: Same as Fig. 4.5 but for the <sup>12</sup>CO 10–9 (*top* panel) and 16–15 (*bottom* panel) transitions.

associated with the intensity ratios of the intermediate- and high-mass YSOs respectively.

To obtain these ratios, the spectra of each set of water transitions for a given source are resampled to 1 km s<sup>-1</sup> bins. Then, the studied line (either the 752 or 1097 GHz transition) is divided by the spectrum of the 988 GHz line within the range of velocities over which the intensities of both lines are above 3 $\sigma$  of the re-binned data. Finally, the red and blue wings are averaged together and the obtained intensity ratio as a function of velocity is averaged over all sources that compose each sub-sample of YSOs. Only velocity ranges well offset from the quiescent envelope emission are plotted, typically  $|v - v_{\text{LSR}}| > 3\text{--}5$  km s<sup>-1</sup>.

As found for the low-mass Class 0 protostars, the line intensity ratios seem to be constant as a function of velocity for both intermediate- and high-mass YSOs. This result confirms the fact that the shape of the three water line profiles is similar for a given source and just scales in intensity (Fig. 4.1, right). For the high-mass objects, the ratio increases slightly for offset velocities  $> 25$  km s<sup>-1</sup>. However, the significance of the increase in the ratio is of the order of the uncertainty of those channels. The  $2_{11-2_{02}} / 2_{02-1_{11}}$  ratio is above 1 for this sub-sample of objects at all velocities, which is consistent with the result obtained in the previous sub-section for this set of water lines. A constant line ratio as a function of velocity rules out the optically thick LTE solution for all lines as this would require high column densities even at high velocities, and thus a flatter line profile than observed, or high opacity across the entire profile.

A different outcome is obtained if the CO line intensity is compared to that of water as a function of velocity. Figure 4.6 shows the <sup>12</sup>CO  $J = 10\text{--}9$  and  $J = 16\text{--}15$  over the H<sub>2</sub>O  $2_{02-1_{11}}$

(988 GHz) line ratio as a function of velocity offset (top and bottom panel respectively). In this case, we observe two different behaviours for the two sub-samples of YSOs. For the low-mass Class 0 protostars the  $^{12}\text{CO } J = 10-9 / \text{H}_2\text{O } 2_{02-1_{11}}$  line ratio decreases with velocity, while the  $^{12}\text{CO } J=16-15 / \text{H}_2\text{O } 2_{02-1_{11}}$  ratio is invariant with velocity.

On the other hand, for the high-mass YSOs the line ratio of both CO transitions with  $\text{H}_2\text{O } 2_{02-1_{11}}$  is constant with velocity. This agrees with the ratio of the  $FWZI$  and  $FWHM_b$  for these two molecules being close to unity (see red crosses in Figs. 4.2 and 4.14). Therefore, in massive objects the emission of these CO and water transitions may originate in regions of the outflow cavity wall not too distant from each other and characterised by similar excitation and dynamical conditions. For the low-mass Class 0 sources, the  $^{12}\text{CO } 16-15$  line seems to trace the same material as  $\text{H}_2\text{O}$  but the  $10-9$  transition does not (Kristensen et al. in prep.).

### 4.3.6. Excitation conditions

In order to characterise the excitation conditions responsible for the broad cavity shock water emission, we compared the line fluxes presented above, together with the fluxes for the  $1_{11}-0_{00}$  transition from M<sup>c</sup>Coe et al. in prep. and van der Tak et al. (2013), for the intermediate and high-mass YSOs to a grid of non-LTE RADEX (van der Tak et al. 2007). We use the assumption of a 1-D slab geometry and the same modifications and parameters as used by Mottram et al. (2014) for the low-mass cavity shock components.

We find a good fit with post-shock volume densities  $n_{\text{H}_2} = 10^5 - 4 \times 10^6 \text{ cm}^{-3}$  and water column densities  $N_{\text{H}_2\text{O}} = 10^{17} - 10^{18} \text{ cm}^{-2}$  for 5/7 of the intermediate-mass sources. The results for NGC7129 are shown as an example in the top panels of Fig. 4.7. These results are similar to lower-density solution obtained for the low-mass sources by Mottram et al. (2014) but with slightly larger emitting regions sizes, equivalent to radii of 300–500 AU if circular. All studied water transitions are optically thick but effectively thin in these conditions. In one of the remaining two intermediate-mass sources (L1641 S3MMS1) we cannot constrain the fit very well, while for the other source (NGC2071) a good fit cannot be found within the grid ( $\chi^2_{\text{best}} > 100$ ), with the emission in the  $2_{11}-2_{02}$  line underproduced and emission in the  $1_{11}-0_{00}$  line overproduced by the models. For the high-mass YSOs, good fits can only be found for 6 of the 19 sources, with the best fits again giving similar densities and column densities and emitting regions ranging from 800 to 6000 AU. However, even in these cases the best-fit models consistently underproduce the  $2_{11}-2_{02}$  transition.

In order to explore what is required to find a good solution for the high-mass sources, we first ran additional grids of models for the poorly fit source G10.47+0.03 where the kinetic temperature was increased from the default of 300 K, but no better solutions were found even at 1500 K. The fact that the same temperature leads to reasonable results for the cavity shock component across the luminosity range is consistent with the results of Karska et al. (2014a), who find similar rotational temperatures for warm CO emission observed with PACS for both low- and high-mass sources.

As an alternative, we also explored pumping by an infrared radiation field with the same shape as the source SED from van der Tak et al. (2013), scaled assuming that the source of infrared radiation is at certain distance away from the water emitting region. Such an approach was found by Mottram et al. (2014) to be inconsistent with the observations of low-mass protostars, but González-Alfonso et al. (2014) find that this is needed to reproduce  $\text{H}_2\text{O}$  observations towards some galaxies. For the high-mass YSO G10.47+0.03, we find that pumping by infrared photons can indeed provide a better fit to the data (see middle and lower panels of Fig. 4.7). This result is consistent with previous works based on observations of vibrational excited molecules such as  $\text{HC}_3\text{N}$  and  $\text{HCN}$  (Wyrowski et al. 1999; Rolfs et al. 2011). We explored a range of distances between the source of the infrared radiation and the  $\text{H}_2\text{O}$  emitting region, from 10 to 1000 AU, and find the best fit for a distance of  $\sim 100$  AU. The best fit for this strong radiation field has both high densities ( $\sim 10^9 - 10^{11} \text{ cm}^{-3}$ ) and column densities ( $\sim 10^{18} \text{ cm}^{-2}$ ) for emitting regions with sizes of order 500 AU. The implications and reasonableness of these results will be discussed further in Sect. 4.4.2.

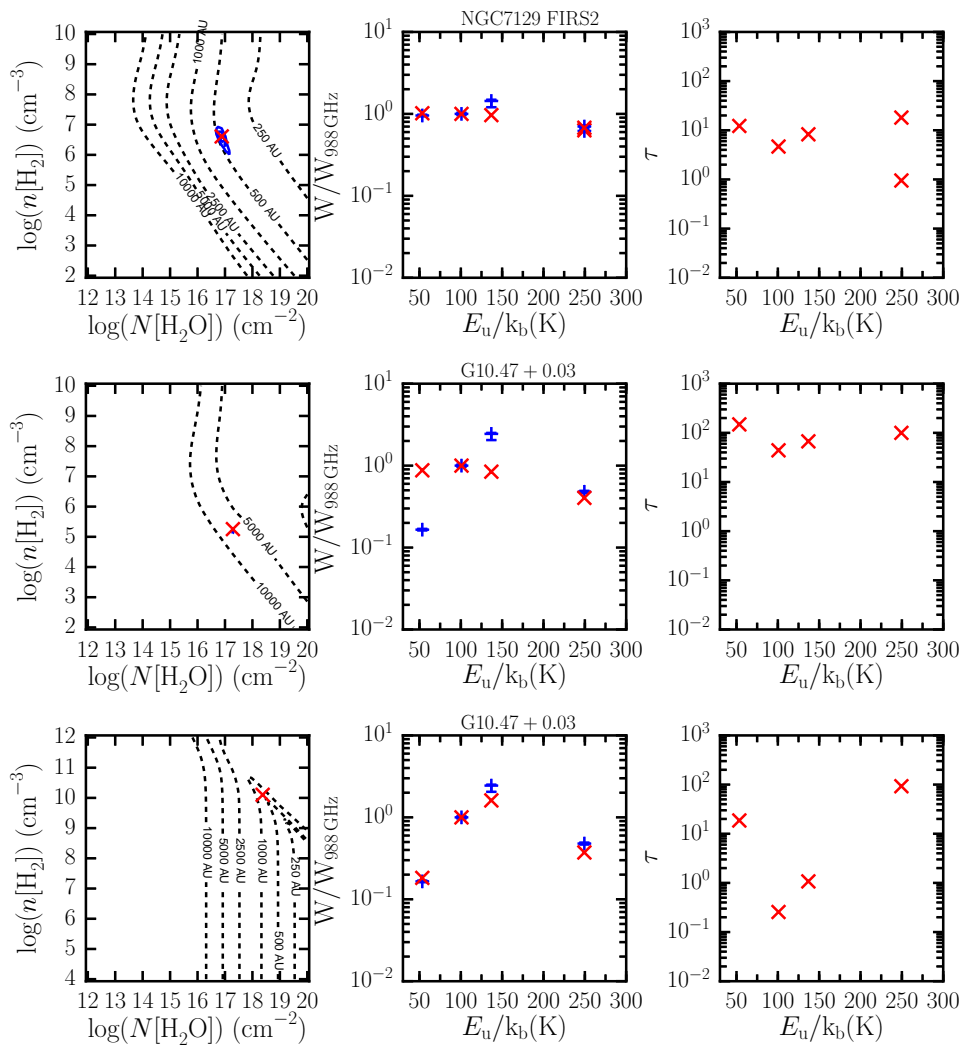


Figure 4.7: RADEX results for the average line ratios for the cavity shock components assuming a kinetic temperature of  $T = 300$  K. The *top* panels corresponds to the intermediate-mass object NGC7129 FIRS2 in which no radiation field has been included. The *middle* and *bottom* panels show the results for the high-mass YSOs G10.47+0.03 without and with radiation field respectively. For each row, the *left-hand* panels show the best-fit (red cross), the 1, 3 and  $5\sigma$  confidence limits (blue contours) for a grid in  $n_{\text{H}_2}$  and  $N_{\text{H}_2\text{O}}$  and the side of the emitting region (black dashed lines). The *middle* panels show a spectral line energy distribution comparing the observed and best-fit model with blue plus and red cross symbols, respectively. Finally, the *right-hand* panels present the optical depth,  $\tau$ , of the best-fit model for each  $\text{H}_2\text{O}$  line.

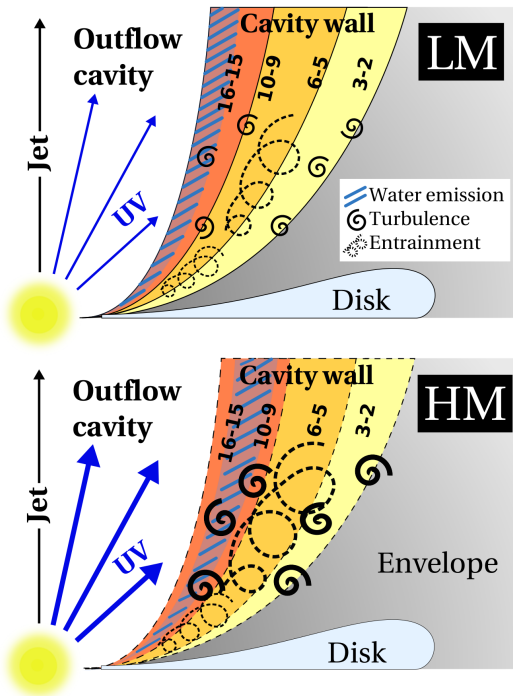


Figure 4.8: Cartoon illustrating a scenario with a simplified physical structure of the different layers composing the outflow cavity wall for a representative low-mass protostar (LM; *top* panel) and for a high-mass YSO (HM; *bottom* panel). The emitting area of the low- $J$   $^{12}\text{CO}$  transitions is shaded in yellow, that of the mid- $J$  transitions is orange and of the high- $J$  lines in red. Turbulent motions are represented with spiral symbols, the entrained material with swirls and the excited water emission is indicated with blue lines over the red region.

## 4.4. Discussion

### 4.4.1. Disentangling the dynamical properties of $\text{H}_2\text{O}$ and $\text{CO}$ emission

The data presented in Sect. 4.3 suggest that  $\text{H}_2\text{O}$  appears in a different physical component from some of the  $\text{CO}$  lines. It is now well established that the broad component seen in low- ( $J < 5$ ) and mid- $J$  ( $5 \leq J < 10$ )  $^{12}\text{CO}$  lines probes the colder entrained outflow gas, whereas only the high- $J$  ( $J > 10$  or higher)  $^{12}\text{CO}$  transitions trace the currently shocked gas also seen in water (van Kempen et al. 2009a, 2010; Nisini et al. 2010; Santangelo et al. 2012; Tafalla et al. 2013; Goicoechea et al. 2012; Yıldız et al. 2013; San José-García et al. 2013). The cartoon presented in Fig. 4.8 illustrates a simplified version of a possible framework for the origin of  $^{12}\text{CO}$  (yellow, orange and red areas) and water (blue lines and opaque region) within the outflow cavity wall for a low- (LM) and high-mass (HM) YSO. Turbulent motions, likely driven by the outflow (San José-García et al. 2013, San José-García et al. *subm.*) are represented with spiral symbols and the entrainment with swirls.

The yellow areas are related to colder layers of the outflow cavity wall directly attached to the envelope where the broad velocity component of low- $J$   $^{12}\text{CO}$  transitions originates. The orange regions are associated with warmer entrained outflowing material within the outflow cavity wall and the red areas indicate material that is currently mixing and undergoing shocks along the outflow cavity. Finally, the velocity of the layers forming the outflow cavity wall and the temperature of the gas decrease with distance from the cavity and the central source (Raga & Cantó 1997). The shocked gas along the layers closest to the outflow cavity should have larger average velocities than that originating near the envelope.

In this context, Fig. 4.2 (and Fig. 4.14) shows that the values of  $FWZI$  for the  $\text{H}_2\text{O}$  and high- $J$   $^{12}\text{CO}$  observations behave differently with  $L_{\text{bol}}$ . For the low-mass protostars, the gas probed by  $\text{H}_2\text{O}$  along the outflow cavity is characterised by larger velocities than the warm entrained outflowing material traced by  $^{12}\text{CO}$   $J = 10-9$ . In addition, the decrease of the  $^{12}\text{CO}$   $J = 10-9$  and  $\text{H}_2\text{O}$   $2_{02}-1_{11}$  ratio as a function of velocity (Fig. 4.6) suggests that these two transitions are kinematically distinct, and originate in different layers of the outflow cavity wall. On the other

hand, the ratio of the CO 16–15 /  $2_{02-111}$  line intensity is constant with velocity, so water and  $^{12}\text{CO}$  16–15 emission go together along the outflow cavity wall.

For the high-mass YSOs, the velocity of the gas traced by  $\text{H}_2\text{O}$  and high- $J$   $^{12}\text{CO}$  transitions are similar, as shown by the bottom panel of Fig. 4.2, and the line intensity ratio of these two species is constant as a function of velocity for both the  $^{12}\text{CO}$   $J = 10-9$  and 16–15 transitions. This implies that already the emission of the  $^{12}\text{CO}$   $J = 10-9$  comes from a region with similar dynamical properties to those of water, contrary to what it was measured for their low-mass counterparts. In the following we will discuss two scenarios to explain these results.

The first scenario is based on the fact that high-mass objects have larger UV fields than those measured for their low-mass counterparts (Stäuber et al. 2007). The strong UV radiation would principally destroy water molecules in the warmer layers of the outflow cavity wall closer to the cavity because colder entrained material will be shielded. Therefore, water may be effectively photo-dissociated (and photo-desorbed) deeper into the outflow cavity wall for high-mass objects than for low-mass protostars. CO molecules are not as easily photo-dissociated as  $\text{H}_2\text{O}$ , but still the destruction of CO will be more efficient in the layers nearest to the outflow cavity. This means that the emission from the faster shocked gas which causes broader  $\text{H}_2\text{O}$  line profiles is destroyed for higher mass sources and that emission originating in regions closer to the entrained layer, moving at slower velocities, may survive.

Due to the weaker UV fields, the photo-dissociation of water molecules along layers closer to the outflow cavity is less efficient for low-mass protostars. Therefore, a larger percentage of fast shocked gas emission along the regions closest to the cavity may survive, emission which contributes to the broadening of the line-wings (quantitative models in Visser et al. 2012).

An alternative scenario is based on the fact that the protostellar environments of high-mass YSOs are more turbulent than those of their low-mass counterparts (see Herpin et al. 2012, San José-García et al. 2013, San José-García et al. subm. and bottom panel of Fig. 4.8). Outflow systems inject turbulent motions into the structure forming the outflow cavity wall and these motions could propagate to other physical components of the protostellar system such as the entrained outflowing material. In this case, the material from both components may have a high level of mixing and the separation between the entrained and shocked material within the outflow cavity wall would not be as clearly delineated as for the low-mass protostars. Since the turbulent motions in low-mass protostars are weaker, the different layers constituting the cavity wall are better defined. Thus, the kinematical properties of each  $J$  transition are better differentiated and the emission of CO  $J = 10-9$  material is separated from that originating in shocked water gas along the cavity. Therefore, the dynamical properties of these two structures would be more closely linked for the high-mass YSOs than for their less massive counterparts, being harder to disentangle. This could explain why the calculated ratio of the  $FWZI$  or  $FWHM_b$  for the  $^{12}\text{CO}$   $J = 10-9$  and  $\text{H}_2\text{O}$  profiles is around 1 for the high-mass sub-sample but is lower than 1 for their less massive counterparts.

Finally, we can rule out that high-mass YSOs are analogous to low-mass Class I protostars, for which the line profiles are narrower due to decreased wind velocities (c.f. Kristensen et al. 2012; Mottram et al. 2014). The high-mass sources considered here are closer to the low-mass Class 0 objects in terms of evolutionary stage: the ratios of the envelope mass to gravitational stellar mass,  $M_{\text{env}}/M_g$ , for the high-mass YSOs are  $>20$  (San José-García et al. subm.). Massive YSOs are therefore still deeply embedded and follow the relation with luminosity of the Class 0 rather than to the Class I low-mass sources.

#### 4.4.2. Excitation condition across the luminosity range

As discussed in Sect. 4.3.6, the excitation conditions of water in low- and intermediate-mass sources seem to be similar, while for high-mass YSOs it is difficult to reproduce the observed line ratios, particularly those involving the  $2_{11}-2_{02}$  line (752 GHz). One solution, as discussed in that section, may be that the lines are pumped by infrared radiation in high-mass sources, a process probably not present in low- and intermediate-mass objects due to lower intensity and higher dust extinction within the outflow cavity. However, the best-fit excitation conditions obtained for the high-mass source G10.47+0.03 with the inclusion of a radiation field require very high densities,

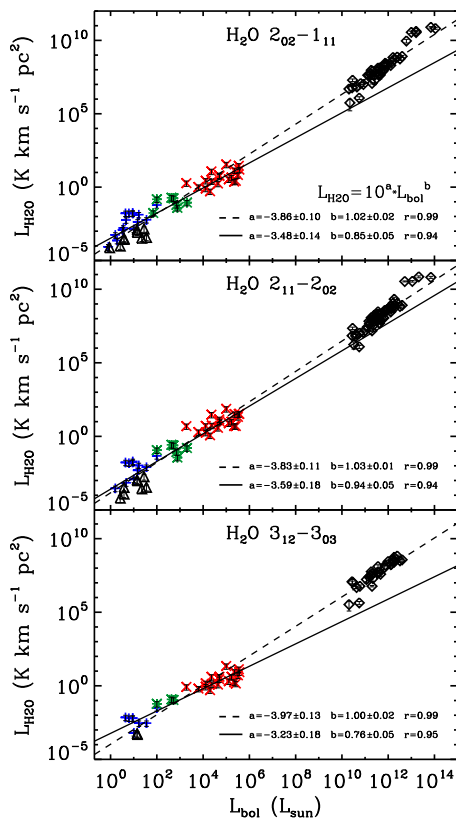


Figure 4.9: Same as Fig.4.3 but including the line luminosity observed for several extragalactic sources (black diamonds) taken from Yang et al. (2013). The solid black line corresponds to the fit of the WISH YSOs and the dashed black line indicates the correlation including the values of extragalactic sources.

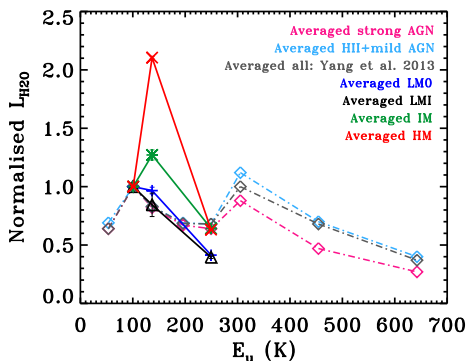


Figure 4.10: Line luminosity of the water transitions normalised to the luminosity of the  $\text{H}_2\text{O } 2_{02}-1_{11}$  (988 GHz) line as a function of the upper energy level ( $E_u$ ) of each transition. The solid blue, black, green and red lines corresponds to the averaged value of the normalised intensity for the low-mass Class 0, Class I, intermediate-mass and high-mass YSOs respectively. The grey dashed line represents the average values of the sample presented in Yang et al. (2013), the pink and light blue dashed lines indicate the values of the strong AGN- and HII+mild-AGN- dominated galaxies, respectively. The  $2_{11}-2_{02}$  (752 GHz) line has an  $E_u/k_B = 137$  K and the  $3_{12}-3_{03}$  (1097 GHz) an  $E_u/k_B = 249$  K.



enough that water emission should be in LTE, over considerable regions. Note that from the grid without radiative pumping we can rule out that high densities alone can reproduce the observed water line ratios. The regions around these high-mass YSOs undoubtedly have a complex geometry and in several cases, including G10.47+0.03, are known to harbour multiple sources within the *Herschel* beam. Therefore, the assumption of a slab geometry, while instructive, may not accurately constrain the range of excitation conditions present. In addition, we have only performed a limited test using a scaled version of the SED as the radiation field, while the “true” radiation field irradiating the water emitting gas in these regions may include shorter-wavelength photons. Furthermore, we assume all the gas is irradiated by the same radiation field, when the geometry of the water emitting region could lead to variation in the field experienced by different parts of the gas.

With all these caveats, we therefore can conclude two things. Firstly, the excitation of water in most high-mass sources is different to low- and intermediate-mass objects. Secondly, while radiative pumping can be ruled out in low-mass protostars, it is a plausible explanation for high-mass sources. Higher kinetic temperatures do not lead to strong enough emission in the  $2_{11}$ - $2_{02}$  transition, in agreement with the similarity of CO rotational temperatures obtained from PACS observations for both low- and high-mass YSOs.

#### 4.4.3. From Galactic to extragalactic sources

San José-García et al. (2013) found that the correlation between the logarithms of the  $^{12}\text{CO}$   $J = 10$ – $9$  line luminosity and  $L_{\text{bol}}$  for the WISH sample held when they extended their analysis to include a sample of extragalactic sources. Similarly, we investigate if the significant correlation measured between the logarithm of the water luminosities,  $L_{\text{H}_2\text{O}}$ , and  $L_{\text{bol}}$  continues in the regime of extragalactic sources.

Figure 4.9 shows the values of  $L_{\text{H}_2\text{O}}$  for a series of AGN and other extragalactic objects presented in Yang et al. (2013). A correlation between the logarithm of these parameters, which extends over more than 12 orders of magnitude in both axis, is measured for the three transitions. The value of the slope is the same for each  $\text{H}_2\text{O}$  line and is equal to 1, which in the case of the  $3_{12}$ - $3_{03}$  transition is slightly larger than the slope obtained considering only the WISH sample. Therefore, if the extragalactic sources are added, the proportionality between the logarithms of the line luminosity and  $L_{\text{bol}}$  is emphasised for all water lines and the slope becomes unity within the uncertainties, as for the  $^{12}\text{CO}$   $J = 10$ – $9$  analysis of San José-García et al. (2013). As previously discussed in Sect 4.3 of that paper, this result suggests that high- $J$  CO can be used as a tracer of dense gas, similar to HCN (Gao & Solomon 2004a,b). From Fig. 4.9 we can conclude that the excited water transitions are also probing dense gas.

The line intensity ratios of these parameters are calculated for the three water lines with respect to the  $2_{02}$ - $1_{11}$  transition (see Fig. 4.10). The results are presented in the context of the extragalactic framework by comparing the excitation conditions of low-, intermediate- and high-mass YSOs to those investigated in the extragalactic sources discussed in Yang et al. (2013).

Surprisingly, the 752 GHz / 988 GHz line intensity ratio only lies above 1 for the high-mass YSOs. This peculiar result, already highlighted within our studied sample of YSOs, also stands out when the line ratios are compared with those measured for extragalactic sources. However, as discussed in Sect. 4.4.2, the modelling used in this paper is quite simple and is only for lines with  $E_u \lesssim 250$  K. Better characterisation of the excitation conditions of more  $\text{H}_2\text{O}$  lines than modelled here is therefore required to conclusively interpret this result.

The fact that the slope of the correlation between  $L_{\text{H}_2\text{O}}$  and  $L_{\text{bol}}$  (Fig. 4.9) gets closer unity after including the extragalactic sources and that the dashed line intercepts the high-mass YSOs (while dropping below their low-mass counterparts) might suggest a plausible scenario in which the extragalactic  $\text{H}_2\text{O}$  emission comes from ensemble of high-mass sources. However, a more fundamental question is whether the extragalactic emission comes from star formation, PDRs, AGN or some combination thereof. Once there is better understanding of where extragalactic water emission originates, further progress can be made on comparing to our galactic observations such as those presented in this paper.

## 4.5. Conclusions

From the analysis of excited H<sub>2</sub>O and high- $J$  <sup>12</sup>CO observations across the entire WISH sample of YSOs we derive the following conclusions:

- The shape of the H<sub>2</sub>O 2<sub>02</sub>-1<sub>11</sub>, 2<sub>11</sub>-2<sub>02</sub> and 3<sub>12</sub>-3<sub>03</sub> line profiles for a given source are similar but scaled in intensity. In addition, their averaged line intensity ratios are constant with increasing offset from the source velocity. These results suggest that the dynamical properties probed by the three water transitions are similar for a given source.
- $FWZI$  and  $FWHM_b$  change little between low- and high-mass YSOs for the H<sub>2</sub>O spectra, while the  $FWZIs$  of the <sup>12</sup>CO  $J = 10-9$  and  $3-2$  transitions increase slightly with  $L_{bol}$ . For both molecules, there is significant scatter in the values of  $FWZI$  and  $FWHM_b$  over the studied luminosity interval, particularly in the case of water ( $FWZI$  ranges from 15 to 189 km s<sup>-1</sup>).
- This scatter, related to the intrinsic properties of the sources, is reduced when the ratio of the <sup>12</sup>CO and H<sub>2</sub>O  $FWZI$  (or  $FWHM_b$ ) is considered. The averaged ratio of their  $FWZI$  increases with  $L_{bol}$  ranging from 0.5 for the low-mass protostars to 1.9 for their massive counterparts. This suggests that for low-mass protostars the entrained material traced by the wings of the <sup>12</sup>CO  $J = 10-9$  (and lower- $J$  lines) is kinematically different to that traced by water in the cavity shocked gas (Kristensen et al. in prep.). In the case of the high-mass YSOs, the CO  $J = 10-9$  emission is already coupled to that of water, so both may come from the same layer of the outflow cavity wall (Fig. 4.8).
- The line intensity ratio of <sup>12</sup>CO  $J = 10-9$  to water decreases with increasing velocity for low-mass YSOs but is approximately constant for high-mass YSOs. However, the line intensity ratio of <sup>12</sup>CO  $J = 16-15$  and H<sub>2</sub>O remains constant for both low- and high-mass YSOs as a function of velocity. This suggests that higher- $J$  <sup>12</sup>CO transitions ( $J > 10$ ) trace deeper warmer layers of the outflow cavity characterised by dynamical properties likely linked to those of the shocked water emission, independently of the mass of the object.
- Two scenarios are proposed to explain the previous result. The first scenario assumes that the increased UV radiation in high-mass YSOs leads to water being more effectively photo-dissociated in those layers of the cavity wall closer to the outflow cavity than for the low-mass protostars. An alternative scenario is also discussed, where the higher turbulence in high-mass star-forming regions, injected by the outflows, propagate into layers of the outflow cavity wall further from the outflow cavity and cause a larger mixing of the material forming those layers than in low-mass protostars. Therefore, the high level of turbulence helps the interaction of warm entrained and cavity shocked material.
- On averaged, more than 60% of the total integrated H<sub>2</sub>O line intensity comes from the cavity shock component for all YSOs. The calculated contribution fractions can be used to interpret and compare velocity resolved and unresolved observations of water.
- The excitation of water for the high-mass YSOs is somewhat different from that of their low- and intermediate-mass counterparts and potentially requires pumping from an infrared radiation field.
- As for CO, the logarithm of the line luminosity for the three water lines strongly correlates with the logarithm of the bolometric luminosity and envelope mass of the object. The slope of the correlation is unity within the uncertainty, which suggests that the size of the water and CO emitting regions scale with luminosity so that the beam filling factor remains the same. This relation also holds when the emission from only the broad cavity shock component is compared.

- The correlation between the total H<sub>2</sub>O line luminosity can be extended to extragalactic sources. In addition, the values of the line intensity ratios of the extragalactic objects are similar to those calculated for the low-mass protostars, but these ratios differ from those measured for the intermediate- and high-mass YSOs.

Overall, despite some differences in excitation, the properties of excited water line emission are similar between low- and high-mass YSOs, suggesting that a common physical mechanism is at work in the outflows of sources across a wide range of luminosity. It remains to be seen whether the scaling relations in line luminosity found here are simply the result of a mass-scaling or whether the outflows of all YSOs are driven in the same way. Resolving this question will require high spatial resolution and fidelity imaging of tracers probing both the entrained and currently shocked outflow material, something ALMA will enable us to do in the coming years for the first time.

## Acknowledgments

The authors are grateful to Sylvie Cabrit for the useful feedbacks that helped to improve the manuscript and to Mihkel Kama for providing data and suggestions to the paper. We would like to thank Umut Yıldız for helping on the data reduction as well as the WISH team for many inspiring discussions. This work is supported by the European Community's Seventh Framework Programme FP7/2007-2013 under grant agreement 238258 (LASSIE) and by the Space Research Organisation Netherlands (SRON). Astrochemistry in Leiden is supported by the Netherlands Research School for Astronomy (NOVA), by a Spinoza grant and grant 614.001.008 from the Netherlands Organisation for Scientific Research (NWO). HIFI has been designed and built by a consortium of institutes and university departments from across Europe, Canada and the United States under the leadership of SRON Netherlands Institute for Space Research, Groningen, The Netherlands and with major contributions from Germany, France and the US. Consortium members are: Canada: CSA, U. Waterloo; France: CESR, LAB, LERMA, IRAM; Germany: KOSMA, MPIfR, MPS; Ireland, NUI Maynooth; Italy: ASI, IFSI-INAF, Osservatorio Astrofisico di Arcetri- INAF; Netherlands: SRON, TUD; Poland: CAMK, CBK; Spain: Observatorio Astronómico Nacional (IGN), Centro de Astrobiología (CSIC-INTA). Sweden: Chalmers University of Technology - MC2, RSS & GARD; Onsala Space Observatory; Swedish National Space Board, Stockholm University - Stockholm Observatory; Switzerland: ETH Zurich, FHNW; USA: Caltech, JPL, NHSC.

## 4.A. Spectra of the excited water lines

The  $\text{H}_2\text{O}$   $2_{02}-1_{11}$ ,  $2_{11}-2_{02}$  and  $3_{12}-3_{03}$  spectra for the intermediate- and high-mass YSOs and the observation number identification are presented in this section (see Figs. 4.11 to 4.13 and Table 4.6). The basic properties derived from these data, such as the rms of the spectra,  $T_{\text{MB}}^{\text{peak}}$ , integrated intensity and  $FWZI$  are summarised from Table 4.7 to 4.9. In addition, the results from the Gaussian decomposition explained in Sect. 4.2.5 are shown in Tables 4.10 to 4.12.

Table 4.6: Observation identification numbers for the  $\text{H}_2\text{O}$   $2_{02}-1_{11}$ ,  $2_{11}-2_{02}$  and  $3_{12}-3_{03}$  lines of the intermediate- and high-mass YSOs.

Source	$2_{02}-1_{11}$	$2_{11}-2_{02}$	$3_{12}-3_{03}$
<b>Intermediate-mass</b>			
NGC7129 FIRS2	1342191613	1342191747	1342227393
L1641 S3MMS1	1342203147	1342203220	–
NGC2071	1342204503	1342194682	1342227395
Vela IRS17	1342197951	1342201541	–
Vela IRS19	1342197952	1342201540	–
AFGL490	1342204511	1342217717	–
OMC-2-FIR 4	1342218629	1342194681	1342217719
<b>High-mass</b>			
IRAS05358+3543	1342204510	1342194684	1342206123
IRAS16272-4837	1342203168	1342205845	1342214418
NGC6334-I-1	1342204520	1342205846	1342206386
W43-MM1	1342191616	1342194565	1342194806
DR21-OH	1342195026	1342194574	1342196427
W3-IRS5	1342191612	1342201548	1342201592
IRAS18089-1732	1342215911	1342217712	1342218914
W33A	1342191636	1342191746	1342208090
IRAS18151-1208	1342218211	1342194679	1342218911
AFGL2591	1342195019	1342192335	1342194796
G327-0.6	1342203170	1342205844	1342214424
NGC6334-I-N-1	1342204519	1342205847	1342206384
G29.96-0.02	1342191617	1342194563	1342194807
G31.41+0.31	1342191615	1342194566	1342219241
G5.89-0.39	1342218120	1342217707	1342218917
G10.47+0.03	1342215914	1342217711	1342218915
G34.26+0.15	1342194995	1342215950	1342219245
W51N-e1	1342195014	1342194568	1342196433
NGC7538-IRS1	1342201599	1342201546	1342200760

Table 4.7: Observed and fitted properties of the  $\text{H}_2\text{O}$   $2_{02}-1_{11}$  line for the detected intermediate- and high-mass sources.

Source	rms <sup>a</sup> (mK)	$T_{\text{MB}}^{\text{peak}}$ (K)	$\int T_{\text{MB}} d\omega^b$ (K km s <sup>-1</sup> )	$FWZI$ (km s <sup>-1</sup> )
<b>Intermediate-mass</b>				
NGC7129 FIRS2	18	0.58	9.50 ± 0.02	48
L1641 S3MMS1	23	0.30	6.28 ± 0.03	48
NGC2071	38	3.83	76.98 ± 0.04	108
Vela IRS17	22	0.74	9.97 ± 0.02	63
Vela IRS19	21	0.34	6.23 ± 0.02	72
AFGL490	21	0.44	6.94 ± 0.02	75
OMC-2-FIR 4	28	3.15	52.31 ± 0.04	66
<b>High-mass</b>				
IRAS05358+3543	57	1.93	24.69 ± 0.09	54
IRAS16272-4837	81	1.34	17.34 ± 0.11	39
NGC6334-I-N-1	60	2.25	43.55 ± 0.09	57
W43-MM1	54	1.02	25.99 ± 0.06	84
DR21-OH	73	5.86	29.39 ± 0.11	51
W3-IRS5	95	7.07	88.32 ± 0.12	63
IRAS18089-1732	107	1.27	12.01 ± 0.14	27
W33A	47	2.23	24.13 ± 0.05	63
IRAS18151-1208	96	0.82	4.88 ± 0.12	30
AFGL2591	100	3.41	17.21 ± 0.13	24
G327-0.6	91	3.23	33.50 ± 0.14	51
NGC6334-I-1	106	5.32	69.44 ± 0.14	60
G29.96-0.02	67	5.36	62.34 ± 0.07	66
G31.41+0.31	61	1.41	18.74 ± 0.07	60
G5.89-0.39	67	9.60	265.34 ± 0.07	108
G10.47+0.03	104	3.58	34.75 ± 0.12	39
G34.26+0.15	64	6.08	48.49 ± 0.07	60
W51N-e1	64	6.75	102.12 ± 0.07	81
NGC7538-IRS1	91	5.56	37.20 ± 0.12	24

**Notes.**  $FWZI$  has been calculated by binning the spectra to 3 km s<sup>-1</sup>.

(<sup>a</sup>) In 0.27 km s<sup>-1</sup> bin. (<sup>b</sup>) Integrated over the interval of velocities defined by the  $FWZI$ .

## 4.B. Specific sources

The low-mass Class 0 protostars indicated in Fig. 4.2 are characterised for showing bullet emission in their water profiles. These already studied sources are: L1448-MM, NGC1333 IRAS2A, BHR 71, SerSMM1 and L1157. In the case of the low-mass Class I object IRAS12496, a spot shock component significantly offset from the source velocity is identified in the 988 GHz water

Table 4.8: Observed and fitted properties of the H<sub>2</sub>O 2<sub>11</sub>-2<sub>02</sub> line for the detected intermediate- and high-mass YSOs.

Source	rms <sup>a</sup> (mK)	T <sub>MB</sub> <sup>peak</sup> (K)	∫ T <sub>MB</sub> dv <sup>b</sup> (K km s <sup>-1</sup> )	FWZI (km s <sup>-1</sup> )
<b>Intermediate-mass</b>				
NGC7129 FIRS2	22	0.52	7.76 ± 0.02	48
L1641 S3MMS1	28	0.24	2.69 ± 0.05	22
NGC2071	37	3.78	62.30 ± 0.04	123
Vela IRS17	30	0.82	8.13 ± 0.03	39
Vela IRS19	36	0.41	3.74 ± 0.04	63
AFGL490	100	0.51	22.46 ± 0.03	33
OMC-2-FIR 4	15	1.87	29.92 ± 0.05	69
<b>High-mass</b>				
IRAS05358+3543	44	2.01	27.57 ± 0.05	100
IRAS16272-4837	81	2.37	21.70 ± 0.08	60
NGC6334I-N-1	92	4.38	117.17 ± 0.17	90
W43-MM1	48	2.77	45.14 ± 0.05	108
DR21-OH	68	7.48	104.18 ± 0.07	90
W3-IRSS5	68	9.09	112.14 ± 0.07	105
IRAS18089-1732	68	1.72	15.62 ± 0.07	36
W33A	79	2.76	30.17 ± 0.08	60
IRAS18151-1208	36	0.86	6.41 ± 0.04	40
AFGL2591	37	3.76	21.37 ± 0.04	42
G327-0.6	147	5.19	60.08 ± 0.15	66
NGC6334-I-1	152	9.69	78.44 ± 0.06	117
G29.96-0.02	96	4.05	42.21 ± 0.10	69
G31.41+0.31	74	2.28	23.93 ± 0.08	57
G5.89-0.39	59	10.67	285.22 ± 0.06	144
G10.47+0.03	73	4.47	45.81 ± 0.07	27
G34.26+0.15	225	10.24	93.03 ± 0.10	42
W51N-e1	242	9.46	150.81 ± 0.24	42
NGC7538-IRS1	61	6.97	49.10 ± 0.06	42

**Notes.** FWZI has been calculated by binning the spectra to 3 km s<sup>-1</sup>.

(<sup>a</sup>) In 0.27 km s<sup>-1</sup> bin. (<sup>b</sup>) Integrated over the interval of velocities defined by the FWZI.

 Table 4.9: Observed and fitted properties of the H<sub>2</sub>O 3<sub>12</sub>-3<sub>03</sub> line for the detected intermediate- and high-mass objects.

Source	rms <sup>a</sup> (mK)	T <sub>MB</sub> <sup>peak</sup> (K)	∫ T <sub>MB</sub> dv <sup>b</sup> (K km s <sup>-1</sup> )	FWZI (km s <sup>-1</sup> )
<b>Intermediate-mass</b>				
NGC7129-FIRS2	14	0.46	7.48 ± 0.02	66
L1641 S3MMS1	–	–	–	–
NGC2071	28	2.68	58.82 ± 0.03	117
Vela IRS17	–	–	–	–
Vela IRS19	–	–	–	–
AFGL490	–	–	–	–
OMC-2-FIR 4	30	1.589	25.10 ± 0.11	54
<b>High-mass</b>				
IRAS05358+3543	30	1.20	19.29 ± 0.03	60
IRAS16272-4837	32	0.77	11.11 ± 0.04	42
NGC6334I-N-1	28	1.34	28.34 ± 0.03	90
W43-MM1	24	0.83	13.07 ± 0.03	85
DR21-OH	25	3.66	63.78 ± 0.03	102
W3-IRSS5	81	6.78	99.98 ± 0.08	78
IRAS18089-1732	30	1.04	15.99 ± 0.03	66
W33A	19	1.84	20.24 ± 0.02	66
IRAS18151-1208	30	0.47	5.85 ± 0.03	40
AFGL2591	22	2.54	16.02 ± 0.03	57
G327-0.6	39	1.88	24.97 ± 0.04	57
NGC6334-I-1	128	3.73	48.12 ± 0.12	30
G29.96-0.02	34	2.88	36.15 ± 0.04	81
G31.41+0.31	36	1.28	13.79 ± 0.04	45
G5.89-0.39	36	8.38	237.69 ± 0.04	144
G10.47+0.03	32	2.25	24.35 ± 0.04	27
G34.26+0.15	42	5.01	45.95 ± 0.05	48
W51N-e1	63	4.40	82.48 ± 0.07	110
NGC7538-IRS1	37	3.96	27.53 ± 0.04	81

**Notes.** FWZI has been calculated by binning the spectra to 3 km s<sup>-1</sup>.

(<sup>a</sup>) In 0.27 km s<sup>-1</sup> bin. (<sup>b</sup>) Integrated over the interval of velocities defined by the FWZI.

line in emission but in absorption in the other ground-based transitions. More information about these objects and their observations in Mottram et al. (2014).

The excited water spectra of the intermediate-mass YSO NGC2071 show an offset component at around 35 km s<sup>-1</sup> from the source velocity, which could be considered as a spot shock component, in particular an EHV component. This source is known for being formed by several YSOs, which line profile could be then composed by the emission of several sources and molecular outflows (van Kempen et al. 2012). Therefore, interferometric data is needed disentangle and better understand the emission.

Finally, the line profiles of the high-mass YSO G5.89-0.39 are complex and composed by velocity components with non-Gaussian profiles. As for NGC2071, this region is crowded with several protostars and energetic outflows (Su et al. 2012) with some of the highest velocities measured for these structures (Choi et al. 1993) Therefore, the interpretation of the emission should go together with extra single-dish and interferometric observations.

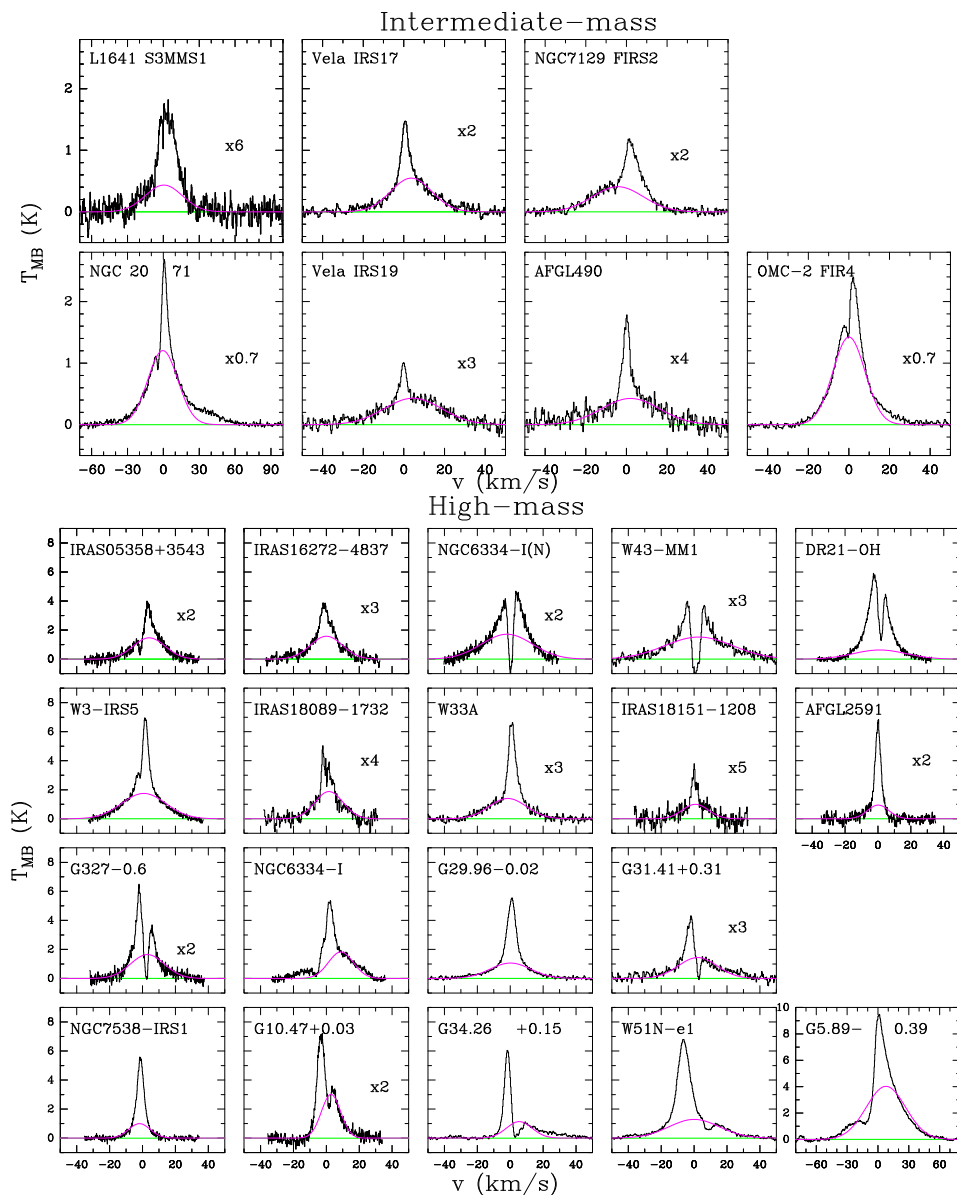


Figure 4.11:  $\text{H}_2\text{O } 2_{02}-1_{11}$  spectra for the intermediate-mass YSOs (*top*) and high-mass sources (*bottom*). The green line represents the baseline level and the pink Gaussian the broad velocity component. All spectra have been shifted to zero velocity. The numbers indicate where the spectra have been scaled for greater visibility.

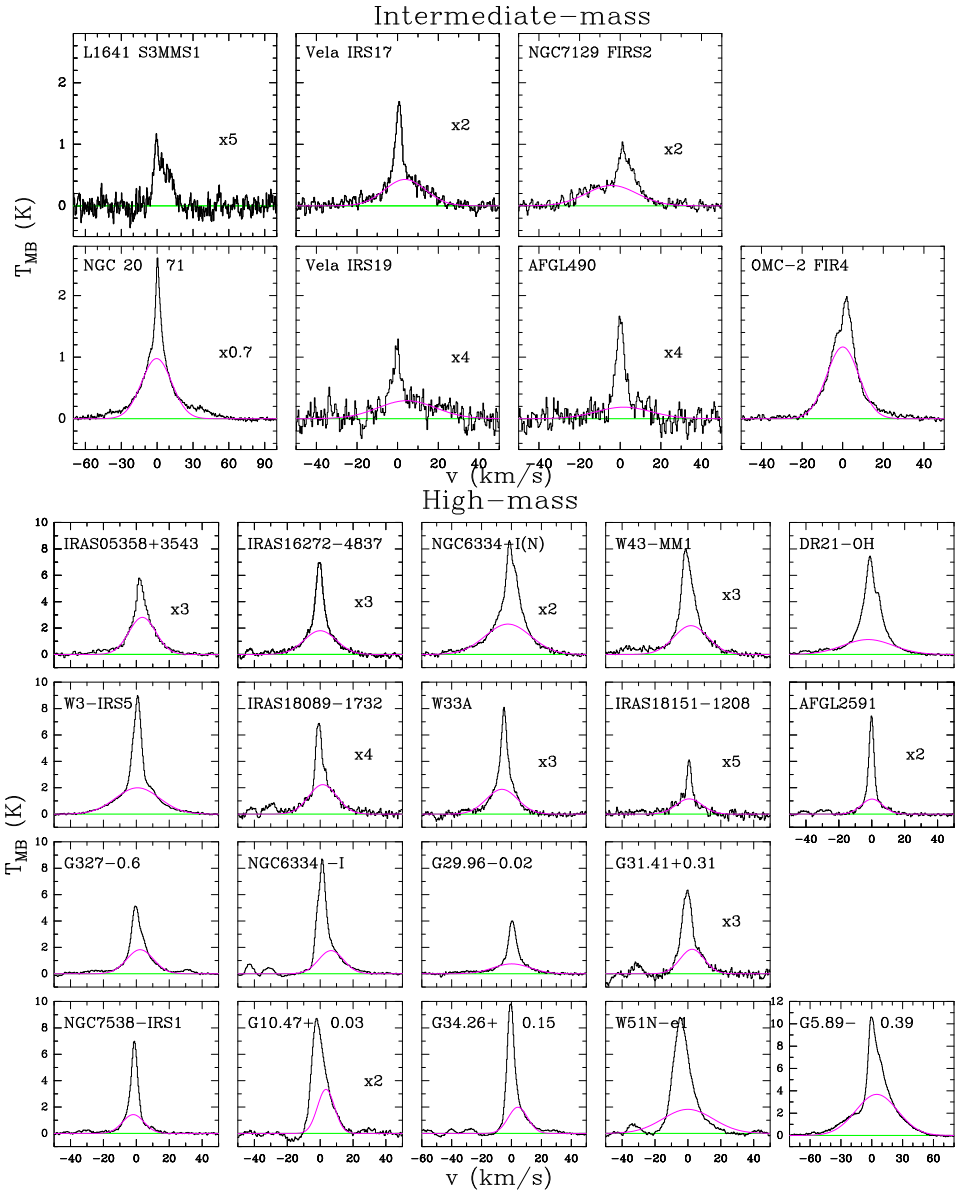


Figure 4.12:  $\text{H}_2\text{O } 2_{11-2_{02}}$  spectra for the intermediate-mass YSOs (*top*) and high-mass sources (*bottom*). The green line represents the baseline level and the pink Gaussian the broad velocity component. All spectra have been shifted to zero velocity. The numbers indicate where the spectra have been scaled for greater visibility.

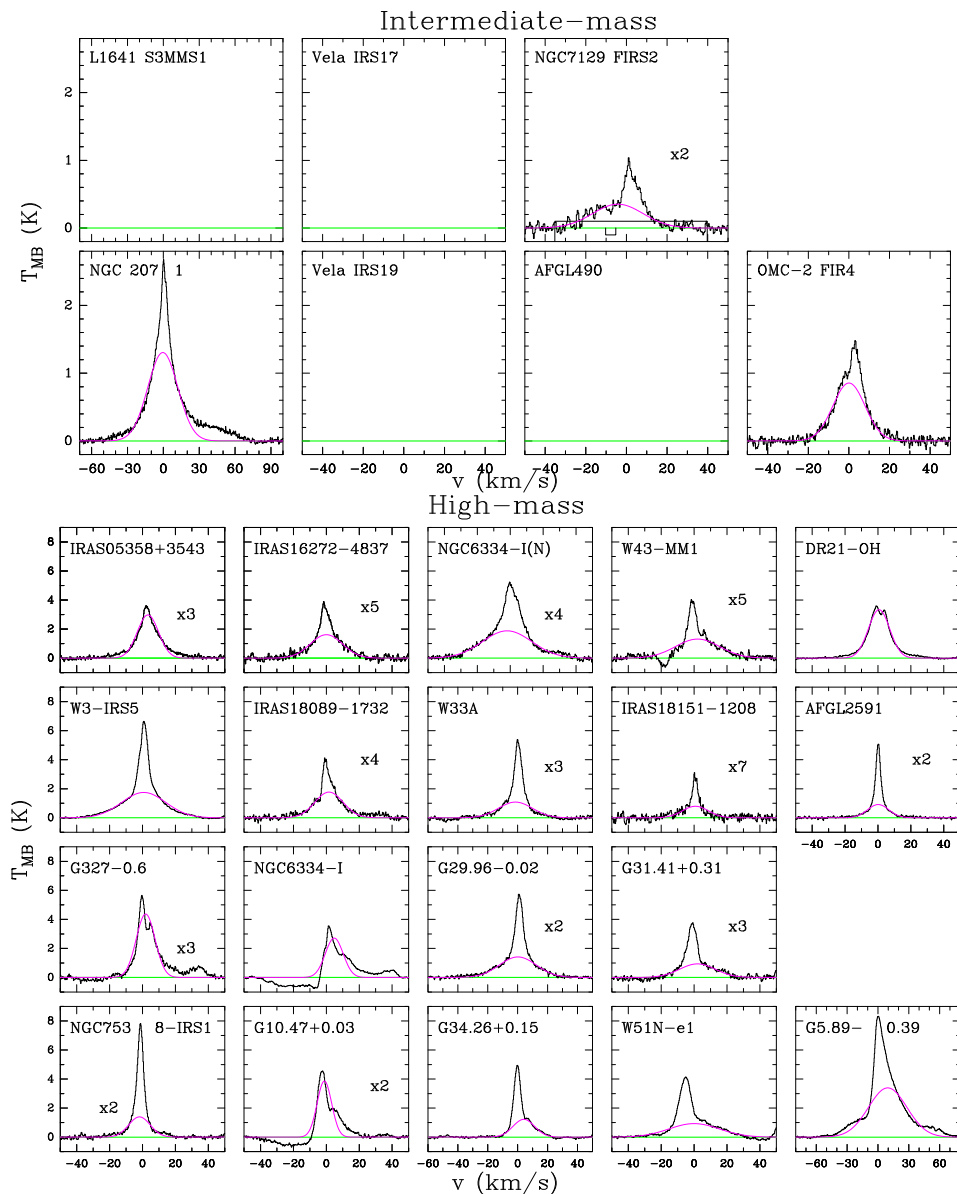


Figure 4.13:  $\text{H}_2\text{O}$   $3_{12}\text{-}3_{03}$  spectra for the intermediate-mass YSOs (*top*) and high-mass objects (*bottom*). The green line represents the baseline level and the pink Gaussian the broad velocity component. All spectra have been shifted to zero velocity. The numbers indicate where the spectra have been scaled for greater visibility.



Table 4.10: Gaussian decomposition results for the intermediate-mass objects.

Source	Comp. <sup>a</sup>	$FWHM_b$ (km s <sup>-1</sup> )	$v_{\text{peak}}$ (km s <sup>-1</sup> )	$v_{\text{LSR}}$ (km s <sup>-1</sup> )	H <sub>2</sub> O 2 <sub>02</sub> -1 <sub>11</sub>		H <sub>2</sub> O 2 <sub>11</sub> -2 <sub>02</sub>		H <sub>2</sub> O 3 <sub>12</sub> -3 <sub>03</sub>	
					$T_{\text{MB}}^{\text{peak}}$ (K)	$\int T_{\text{MB}} dv^b$ (K km s <sup>-1</sup> )	$T_{\text{MB}}^{\text{peak}}$ (K)	$\int T_{\text{MB}} dv^b$ (K km s <sup>-1</sup> )	$T_{\text{MB}}^{\text{peak}}$ (K)	$\int T_{\text{MB}} dv^b$ (K km s <sup>-1</sup> )
NGC7129 FIRS2	C	29.3 ± 0.3	-13.99 ± 0.17	-9.8	0.192 ± 0.004	5.99 ± 0.14	0.160 ± 0.004	4.99 ± 0.13	0.166 ± 0.003	5.18 ± 0.11
	E	8.46 ± 0.11	-7.20 ± 0.04	-9.8	0.368 ± 0.005	3.31 ± 0.06	0.282 ± 0.006	2.54 ± 0.06	0.285 ± 0.004	2.57 ± 0.05
L1641 S3MMS1	C	34 ± 3	6.4 ± 0.9	5.3	0.073 ± 0.013	2.6 ± 0.5	0.084	3.04	-	-
	E	15.3 ± 0.5	8.57 ± 0.16	5.3	0.197 ± 0.014	3.2 ± 0.3	0.155 ± 0.005	2.53 ± 0.11	-	-
NGC2071	C	29.60 ± 0.12	9.14 ± 0.05	9.6	1.722 ± 0.008	54.3 ± 0.3	1.42 ± 0.007	44.7 ± 0.3	1.311 ± 0.006	41.3 ± 0.3
	E	6.122 ± 0.04	10.17 ± 0.02	9.6	2.039 ± 0.017	13.3 ± 0.2	1.924 ± 0.012	12.5 ± 0.1	1.283 ± 0.009	8.36 ± 0.08
	S	31.2 ± 0.7	46.9 ± 0.3	9.6	0.277 ± 0.005	9.2 ± 0.3	0.199 ± 0.004	6.6 ± 0.2	0.229 ± 0.003	7.6 ± 0.2
Vela IRS17	A	3.65 ± 0.09	6.54 ± 0.04	9.6	-0.814 ± 0.018	-3.16 ± 0.11	-	-	-	-
	C	23.8 ± 0.4	7.53 ± 0.14	3.9	0.277 ± 0.005	7.01 ± 0.16	0.158 ± 0.005	4.00 ± 0.14	-	-
	E	4.19 ± 0.07	4.47 ± 0.03	3.9	0.462 ± 0.009	2.06 ± 0.05	0.608 ± 0.011	2.71 ± 0.07	-	-
Vela IRS19	C	33.3 ± 0.8	16.7 ± 0.3	12.2	0.141 ± 0.003	5.00 ± 0.16	0.068 ± 0.004	2.41 ± 0.15	-	-
	E	4.14 ± 0.18	11.92 ± 0.07	12.2	0.183 ± 0.008	0.81 ± 0.05	0.215 ± 0.012	0.95 ± 0.07	-	-
AFGL490	C	31.9 ± 1.0	-11.7 ± 0.4	-13.5	0.107 ± 0.004	3.63 ± 0.18	0.033 ± 0.004	1.12 ± 0.14	-	-
	E	4.56 ± 0.11	-13.40 ± 0.04	-13.5	0.299 ± 0.007	1.45 ± 0.05	0.364 ± 0.011	1.77 ± 0.07	-	-
OMC-2-FIR 4	C	18.62 ± 0.07	11.33 ± 0.03	11.3	2.085 ± 0.018	41.3 ± 0.4	1.210 ± 0.009	24.0 ± 0.2	1.031 ± 0.010	20.4 ± 0.2
	E	6.26 ± 0.08	13.40 ± 0.02	11.3	1.03 ± 0.03	6.87 ± 0.19	0.677 ± 0.009	4.51 ± 0.08	0.566 ± 0.014	3.77 ± 0.11

**Notes.** (<sup>a</sup>) The types of components are: C = cavity shock; E = envelope emission; S = spot shock; A = envelope absorption. (<sup>b</sup>) Integrated intensity of each velocity component approximated to the gaussian fit.

Table 4.11: Gaussian decomposition results for the high-mass YSOs.

Source	Comp. <sup>a</sup>	$FWHM_b$ (km s <sup>-1</sup> )	$v_{\text{peak}}$ (km s <sup>-1</sup> )	$v_{\text{LSR}}$ (km s <sup>-1</sup> )	H <sub>2</sub> O 2 <sub>02</sub> -1 <sub>11</sub>		H <sub>2</sub> O 2 <sub>11</sub> -2 <sub>02</sub>		H <sub>2</sub> O 3 <sub>12</sub> -3 <sub>03</sub>	
					$T_{\text{MB}}^{\text{peak}}$ (K)	$\int T_{\text{MB}} dv^b$ (K km s <sup>-1</sup> )	$T_{\text{MB}}^{\text{peak}}$ (K)	$\int T_{\text{MB}} dv^b$ (K km s <sup>-1</sup> )	$T_{\text{MB}}^{\text{peak}}$ (K)	$\int T_{\text{MB}} dv^b$ (K km s <sup>-1</sup> )
IRAS05358+3543	C	23.0 ± 0.2	-13.56 ± 0.07	-17.6	0.786 ± 0.015	19.2 ± 0.4	0.812 ± 0.014	19.9 ± 0.4	0.550 ± 0.009	13.5 ± 0.3
	E	6.49 ± 0.09	-15.05 ± 0.03	-17.6	1.14 ± 0.03	7.9 ± 0.2	1.079 ± 0.017	7.46 ± 0.16	0.617 ± 0.012	4.26 ± 0.10
	A	3.69 ± 0.14	-18.01 ± 0.06	-17.6	-0.85 ± 0.03	-3.32 ± 0.16	–	–	–	–
IRAS16272-4837	C	23.0 ± 0.4	-46.15 ± 0.13	-46.2	0.531 ± 0.018	13.0 ± 0.5	0.72 ± 0.02	17.5 ± 0.6	0.300 ± 0.008	7.4 ± 0.2
	E	5.61 ± 0.11	-46.78 ± 0.04	-46.2	0.72 ± 0.03	4.3 ± 0.2	1.59 ± 0.03	9.6 ± 0.3	0.420 ± 0.012	2.51 ± 0.09
NGC6334I-N-1	C	36.4 ± 0.3	-5.24 ± 0.08	-3.3	0.803 ± 0.012	31.1 ± 0.5	1.191 ± 0.015	46.1 ± 0.7	0.508 ± 0.006	19.7 ± 0.3
	E	10.41 ± 0.07	-2.99 ± 0.02	-3.3	2.39 ± 0.04	26.5 ± 0.5	2.703 ± 0.018	30.0 ± 0.3	0.763 ± 0.009	8.46 ± 0.12
	A	3.95 ± 0.05	-3.07 ± 0.01	-3.3	-3.60 ± 0.04	-15.2 ± 0.2	–	–	–	–
W43-MM1	C	48.8 ± 0.5	101.65 ± 0.19	98.8	0.429 ± 0.008	22.3 ± 0.5	0.436 ± 0.007	22.7 ± 0.4	0.152 ± 0.003	7.90 ± 0.17
	E	9.10 ± 0.06	98.50 ± 0.02	98.8	1.59 ± 0.09	15.3 ± 0.9	2.150 ± 0.012	20.82 ± 0.18	0.563 ± 0.006	5.45 ± 0.07
	A	5.79 ± 0.12	99.30 ± 0.03	98.8	-2.28 ± 0.08	-14.0 ± 0.6	–	–	–	–
DR21-OH	C	37.6 ± 0.3	-1.99 ± 0.09	-3.1	0.640 ± 0.016	25.6 ± 0.7	0.827 ± 0.017	33.1 ± 0.7	0.629 ± 0.010	25.2 ± 0.5
	E	12.34 ± 0.04	-2.81 ± 0.01	-3.1	5.63 ± 0.03	74.0 ± 0.5	5.46 ± 0.02	71.8 ± 0.3	2.971 ± 0.010	39.04 ± 0.17
	A	3.28 ± 0.03	-1.49 ± 0.01	-3.1	-4.74 ± 0.04	-16.6 ± 0.2	–	–	–	–
W3-IRS5	C	31.57 ± 0.13	-37.62 ± 0.05	-38.4	1.948 ± 0.014	65.5 ± 0.5	2.140 ± 0.013	71.9 ± 0.5	1.976 ± 0.014	66.4 ± 0.5
	E	5.86 ± 0.02	-37.49 ± 0.01	-38.4	4.21 ± 0.03	26.21 ± 0.19	6.55 ± 0.02	40.8 ± 0.2	4.63 ± 0.03	28.84 ± 0.19
IRAS18089-1732	C	20.2 ± 0.3	35.41 ± 0.10	33.8	0.455 ± 0.018	9.8 ± 0.4	0.534 ± 0.015	11.5 ± 0.4	0.459 ± 0.008	9.8 ± 0.2
	E	4.27 ± 0.09	33.30 ± 0.03	33.8	0.58 ± 0.04	2.65 ± 0.18	1.20 ± 0.03	5.47 ± 0.16	0.537 ± 0.012	2.44 ± 0.07
W33A	C	26.8 ± 0.2	36.02 ± 0.08	37.5	0.512 ± 0.008	14.6 ± 0.3	0.728 ± 0.013	20.7 ± 0.4	0.410 ± 0.005	11.68 ± 0.17
	E	5.81 ± 0.03	38.01 ± 0.01	37.5	1.568 ± 0.016	9.70 ± 0.11	1.83 ± 0.03	11.35 ± 0.17	1.347 ± 0.007	8.34 ± 0.07
IRAS18151-1208	C	18.6 ± 0.2	33.6 ± 0.2	32.8	0.220 ± 0.007	4.36 ± 0.15	0.269 ± 0.02	5.33 ± 0.14	0.1 ± 0.3	2.64 ± 0.18
	E	3.3 ± 0.3	32.9 ± 0.3	32.8	0.426 ± 0.015	1.52 ± 0.11	0.57 ± 0.04	2.02 ± 0.17	0.3 ± 0.3	1.1 ± 0.2
AFGL2591	C	15.23 ± 0.17	-5.32 ± 0.05	-5.5	0.48 ± 0.02	7.8 ± 0.4	0.607 ± 0.011	9.8 ± 0.2	0.456 ± 0.007	7.40 ± 0.14
	E	3.50 ± 0.02	-5.48 ± 0.08	-5.5	2.87 ± 0.04	10.7 ± 0.17	3.071 ± 0.016	11.45 ± 0.08	2.006 ± 0.011	7.48 ± 0.06

**Notes.**(<sup>a</sup>) The types of components are: C = cavity shock; E = envelope emission; S = spot shock; A = envelope absorption. (<sup>b</sup>) Integrated intensity of each velocity component approximated to the gaussian fit.

Table 4.12: Gaussian decomposition results for the high-mass YSOs (continuation).

Source	Comp. <sup>a</sup>	$FWHM_b$ (km s <sup>-1</sup> )	$v_{\text{peak}}$ (km s <sup>-1</sup> )	$v_{\text{LSR}}$ (km s <sup>-1</sup> )	H <sub>2</sub> O 2 <sub>02</sub> -1 <sub>11</sub>		H <sub>2</sub> O 2 <sub>11</sub> -2 <sub>02</sub>		H <sub>2</sub> O 3 <sub>12</sub> -3 <sub>03</sub>	
					$T_{\text{MB}}^{\text{peak}}$ (K)	$\int T_{\text{MB}} dv^b$ (K km s <sup>-1</sup> )	$T_{\text{MB}}^{\text{peak}}$ (K)	$\int T_{\text{MB}} dv^b$ (K km s <sup>-1</sup> )	$T_{\text{MB}}^{\text{peak}}$ (K)	$\int T_{\text{MB}} dv^b$ (K km s <sup>-1</sup> )
G327-0.6	C	24.3 ± 0.2	-42.28 ± 0.08	-45.0	0.89 ± 0.02	23.0 ± 0.6	0.616 ± 0.011	15.9 ± 0.3	0.649 ± 0.010	16.8 ± 0.3
	E	6.45 ± 0.06	-44.32 ± 0.02	-45.0	7.4 ± 0.4	51 ± 3	1.618 ± 0.014	11.11 ± 0.14	1.042 ± 0.015	7.16 ± 0.12
	A	4.83 ± 0.07	-43.79 ± 0.03	-45.0	-7.8 ± 0.4	-40 ± 2	–	–	–	–
NGC6334-I-1	C	17.83 ± 0.14	1.43 ± 0.09	-7.4	1.88 ± 0.02	35.7 ± 0.5	1.478 ± 0.014	28.0 ± 0.3	1.76 ± 0.02	33.3 ± 0.5
	E	6.27 ± 0.03	-6.40 ± 0.01	-7.4	4.82 ± 0.07	32.2 ± 0.5	7.31 ± 0.02	48.8 ± 0.3	2.09 ± 0.04	14.0 ± 0.3
	A	2.86 ± 0.10	-7.77 ± 0.04	-7.4	-1.99 ± 0.07	-6.1 ± 0.3	–	–	–	–
G29.96-0.02	C	29.1 ± 0.2	97.74 ± 0.07	97.6	1.059 ± 0.014	32.8 ± 0.5	0.810 ± 0.016	25.1 ± 0.5	0.705 ± 0.008	21.9 ± 0.3
	E	6.20 ± 0.03	98.56 ± 0.01	97.6	4.36 ± 0.02	28.7 ± 0.2	3.13 ± 0.03	20.7 ± 0.2	2.058 ± 0.012	13.58 ± 0.10
G31.41+0.31	C	27.7 ± 0.4	99.62 ± 0.16	97.4	0.413 ± 0.013	12.2 ± 0.4	0.627 ± 0.016	18.5 ± 0.5	0.317 ± 0.008	9.3 ± 0.3
	E	6.73 ± 0.09	96.46 ± 0.03	97.4	1.21 ± 0.04	8.6 ± 0.3	1.65 ± 0.02	11.8 ± 0.2	0.931 ± 0.012	6.67 ± 0.12
	A	4.57 ± 0.16	99.09 ± 0.08	97.4	-1.02 ± 0.03	-4.9 ± 0.2	–	–	–	–
G5.89-0.39	C	45.06 ± 0.05	17.81 ± 0.02	10.0	4.154 ± 0.011	199.2 ± 0.6	4.057 ± 0.009	194.6 ± 0.5	3.474 ± 0.007	166.6 ± 0.4
	E	10.93 ± 0.02	11.62 ± 0.01	10.0	5.564 ± 0.019	64.7 ± 0.3	6.452 ± 0.015	75.1 ± 0.2	4.918 ± 0.010	57.22 ± 0.16
	A	8.92 ± 0.11	1.42 ± 0.05	10.0	-1.741 ± 0.018	-16.5 ± 0.3	–	–	–	–
G10.47+0.03	C	13.79 ± 0.13	70.16 ± 0.11	67.3	1.53 ± 0.03	22.4 ± 0.5	2.162 ± 0.02	31.7 ± 0.5	0.903 ± 0.011	13.3 ± 0.2
	E	5.64 ± 0.06	64.48 ± 0.02	67.3	3.22 ± 0.09	19.4 ± 0.6	3.17 ± 0.05	19.0 ± 0.3	1.67 ± 0.02	10.01 ± 0.16
	A	4.5 ± 0.2	66.95 ± 0.12	67.3	-1.32 ± 0.06	-6.4 ± 0.5	–	–	–	–
G34.26+0.15	C	18.39 ± 0.12	63.52 ± 0.08	58.0	1.186 ± 0.015	23.2 ± 0.3	1.492 ± 0.017	29.2 ± 0.4	1.091 ± 0.010	21.4 ± 0.2
	E	5.50 ± 0.02	57.53 ± 0.01	58.0	52 ± 18	305 ± 109	8.69 ± 0.03	50.9 ± 0.2	3.99 ± 0.02	23.38 ± 0.13
	A	5.60 ± 0.03	57.71 ± 0.07	58.0	-48 ± 18	-286 ± 111	–	–	–	–
W51N-e1	C	36.1 ± 0.2	59.58 ± 0.07	59.5	1.47 ± 0.05	56.27 ± 0.11	1.72 ± 0.02	66.1 ± 0.6	1.28 ± 0.02	49.0 ± 0.4
	E	8.5 ± 0.2	54.30 ± 0.01	59.5	5.31 ± 0.07	47.9 ± 0.7	7.59 ± 0.03	68.5 ± 0.4	3.12 ± 0.03	28.1 ± 0.2
	A	19.4 ± 0.4	62.08 ± 0.14	59.5	-5.2 ± 0.5	-107 ± 9	–	–	–	–
NGC7538-IRS1	C	15.37 ± 0.16	-58.02 ± 0.05	-56.2	1.02 ± 0.03	16.7 ± 0.4	1.37 ± 0.03	22.4 ± 0.5	0.781 ± 0.014	12.8 ± 0.3
	E	4.42 ± 0.02	-57.38 ± 0.01	-56.2	4.51 ± 0.04	21.2 ± 0.2	5.48 ± 0.03	25.77 ± 0.19	3.030 ± 0.018	14.2 ± 0.11

**Notes.** (<sup>a</sup>) The types of components are: C = cavity shock; E = envelope emission; S = spot shock; A = envelope absorption. (<sup>b</sup>) Integrated intensity of each velocity component approximated to the gaussian fit.

## 4.C. Additional figures

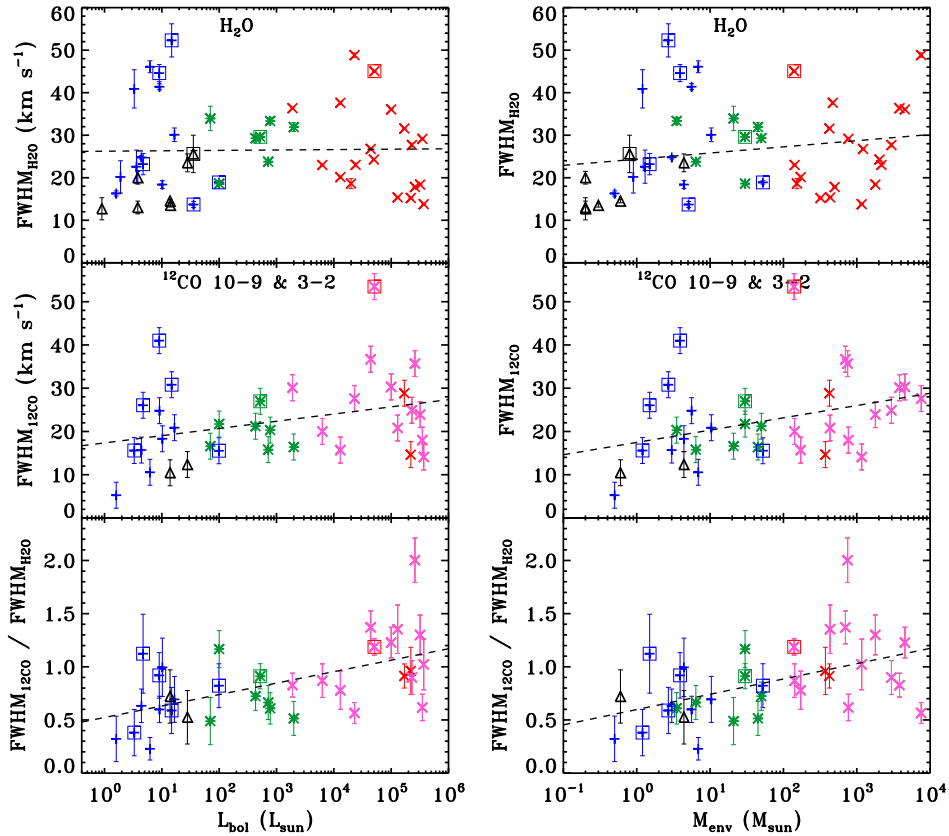


Figure 14.14: (*Left-column figure*) Derived  $\text{FWHM}_b$  of the Gaussian profile fitted to the cavity shock component of the  $\text{H}_2\text{O}$  lines (*top-panel*) as a function of bolometric luminosity. Constrained  $\text{FWHM}_b$  for the  $^{12}\text{CO } J = 10-9$  and  $J = 3-2$  observations (*middle-panel*) versus  $L_{\text{bol}}$ . Ratio calculated from the  $^{12}\text{CO } \text{FWHM}_b$  divided by the  $\text{FWHM}_b$  of the  $\text{H}_2\text{O}$  lines (*bottom-panel*) as a function of  $L_{\text{bol}}$ . (*Right-column figure*) Same as *left-* figure but plotted versus the envelope mass of the source,  $M_{\text{env}}$ . The blue plus symbols correspond to the low-mass Class 0 protostars, the black triangles the low-mass Class I, the green asterisks the intermediate-mass objects, the pink crosses the high-mass YSOs for which the  $^{12}\text{CO } J = 3-2$  spectra are taken, and the red cross symbols the high-mass object for which  $^{12}\text{CO } J = 10-9$  data are available (see San José-García et al. 2013). The low- and intermediate-mass objects with detected EHV components are surrounded by a box. Also the high-mass YSO with triangular water line profiles is surrounded by a box. The value of the  $\text{FWHM}_b$  of the different velocity components is calculated as explained in Sect. 4.2.5 and these parameters are the same for the three water transitions.

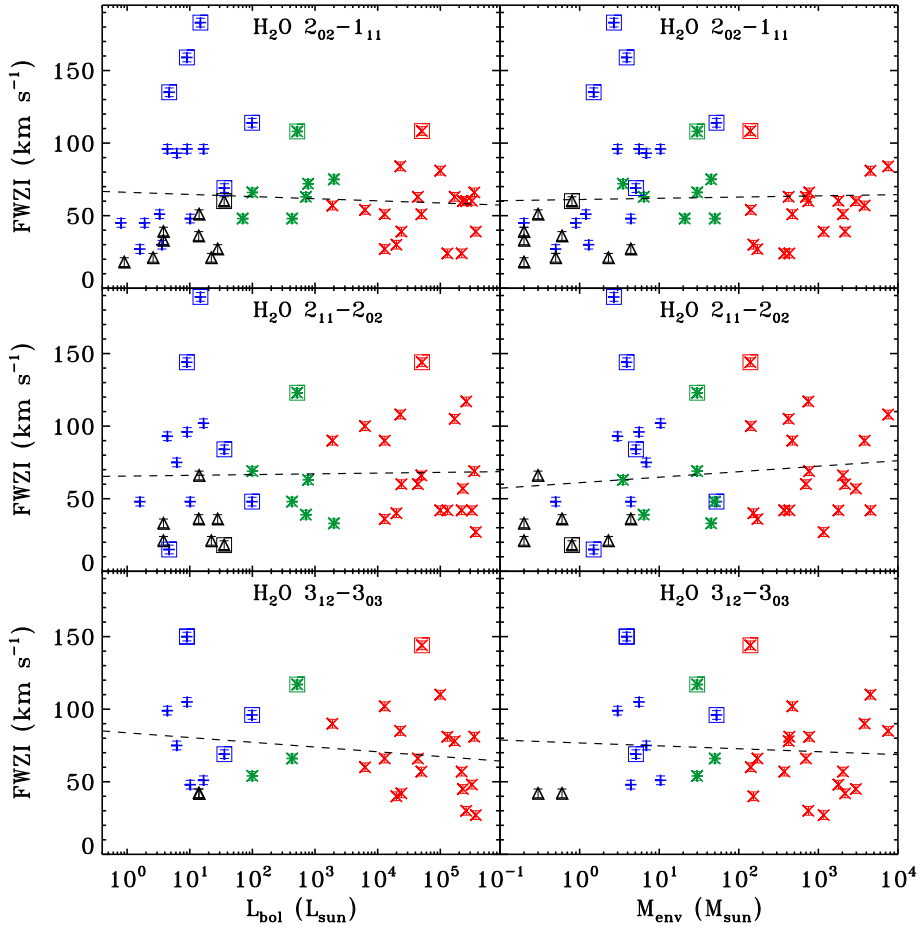


Figure 4.15: (*Left-column*)  $FWZI$  of the  $H_2O$   $2_{02}-1_{11}$  988 GHz (*top panel*),  $2_{11}-2_{02}$  752 GHz (*middle panel*) and  $3_{12}-3_{03}$  1097 GHz (*bottom panel*) transitions as a function of the bolometric luminosity of each source. (*Right-column*) Same as *left-column* but versus the envelope mass of each YSO. The blue plus symbols correspond to the low-mass Class 0 protostars, the black triangles the low-mass Class I, the green asterisks to the intermediate-mass objects and the red crosses to the high-mass YSOs. The low- and intermediate-mass objects with detected EHV components are surrounded by a box, as well as the high-mass YSO with triangular line profiles.  $FWZI$  is calculated by binning the spectra to  $3 \text{ km s}^{-1}$ .

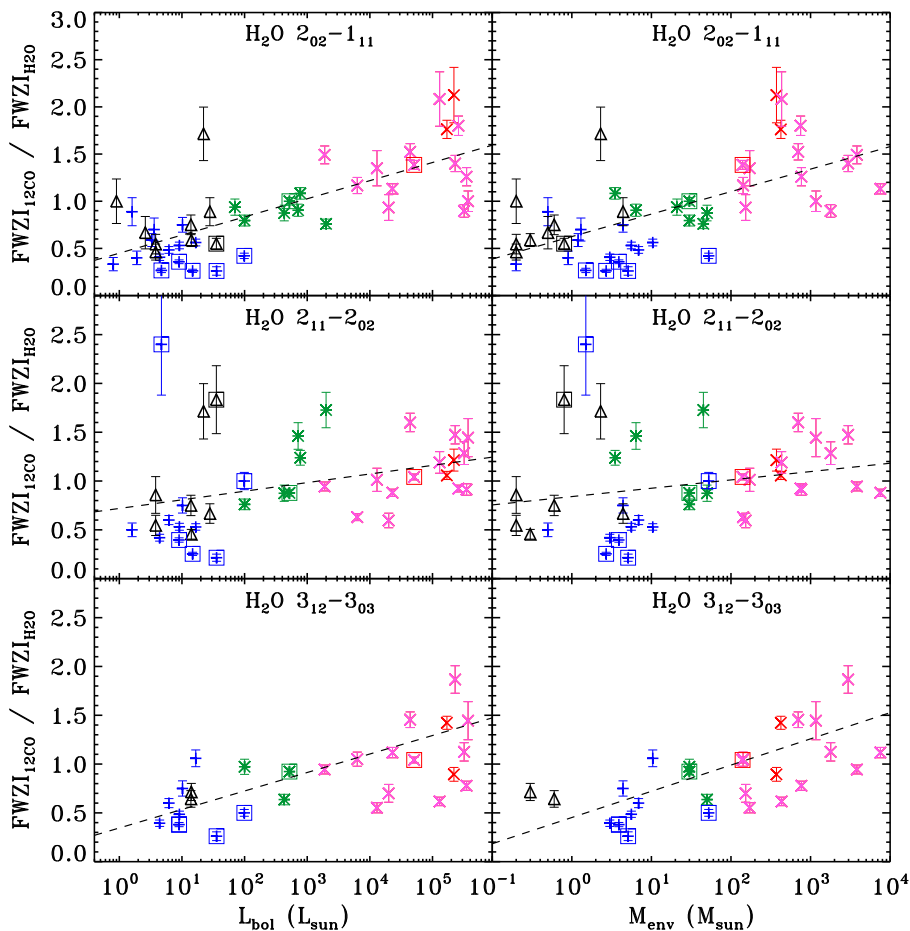


Figure 4.16: (*Left-column*) Ratio of the  $FWZI$  of the  $H_2O$   $2_{02}-1_{11}$  988 GHz (*top panel*),  $2_{11}-2_{02}$  752 GHz (*middle panel*) and  $3_{12}-3_{03}$  1097 GHz (*bottom panel*) transitions and the  $FWZI$  of the  $^{12}CO$  observations as a function of the bolometric luminosity. (*Right-column*) Same as *left-column* but versus the envelope mass of each YSO. The low- and intermediate-mass sources with detected EHV components are surrounded by a box, and also the high-mass YSO with triangular line profiles. Both values of  $FWZI$  were calculated by binning the spectra to  $3 \text{ km s}^{-1}$ . The symbol and colour code is the same as in Fig. 4.2.

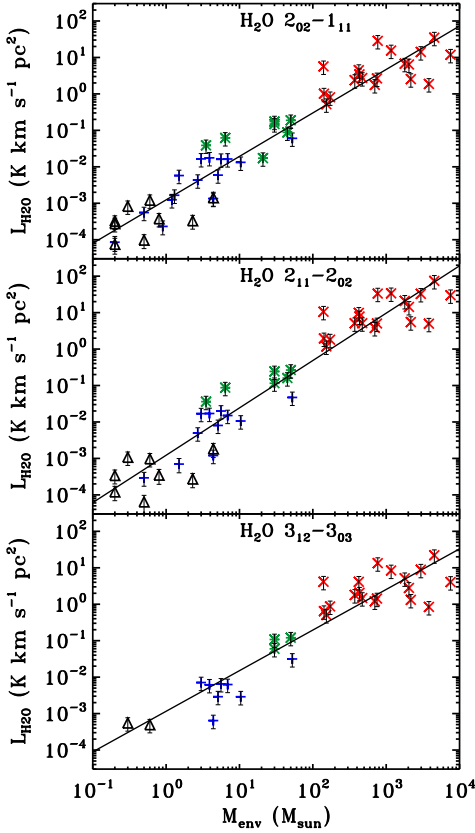


Figure 4.17: Same as Fig. 4.3 but plotted as a function of the envelope mass of the source.

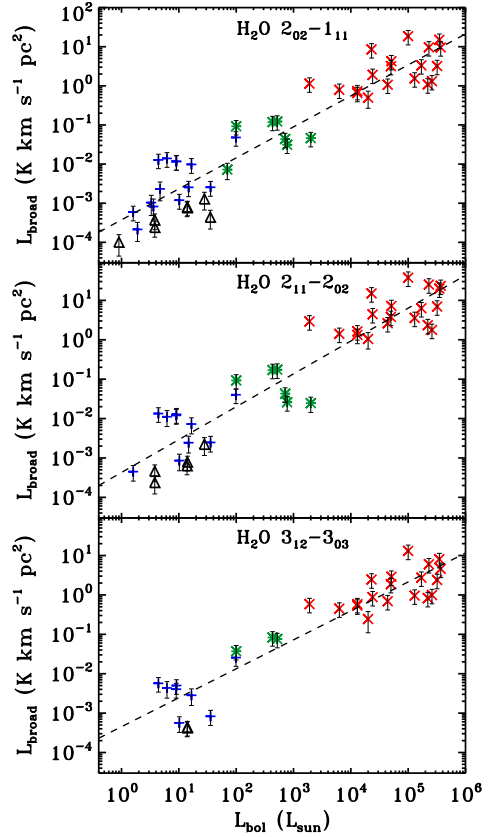


Figure 4.18: Line luminosity of the broad velocity component (emission from shocked gas along the outflow cavity) versus the bolometric luminosity of the source. The symbol and colour code is the same as in Fig. 4.3. The dashed black line shows the log-log correlation of the luminosity measured for the cavity shock emission and  $L_{\text{bol}}$ .

